This is the peer reviewd version of the followng article:

Isotope stratigraphy (87Sr/86Sr, δ18O, δ13C) of the Sorbas basin (Betic Cordillera, Spain): Paleoceanographic evolution across the onset of the Messinian salinity crisis / Reghizzi, Matteo; Gennari, Rocco; Douville, Eric; Lugli, Stefano; Manzi, Vinicio; Montagna, Paolo; Roveri, Marco; Sierro, Francisco Javier; Taviani, Marco. - In: PALAEOGEOGRAPHY PALAEOCLIMATOLOGY PALAEOECOLOGY. - ISSN 0031-0182. - STAMPA. - 469:(2017), pp. 60-73. [10.1016/j.palaeo.2016.12.039]

Terms of use:

The terms and conditions for the reuse of this version of the manuscript are specified in the publishing policy. For all terms of use and more information see the publisher's website.

12/10/2024 11:11

(Article begins on next page)

Palaeogeography, Palaeoclimatology, Palaeoecology 469 (2017) 60–73

Isotope stratigraphy ($^{87}Sr/^{86}Sr$, $\delta^{18}O$, $\delta^{13}C$) of the Sorbas basin (Betic Cordillera, Spain): paleoceanographic evolution across the onset of the Messinian salinity crisis

Reghizzi M. [1, *], Gennari R. [1, 2], Douville, E. [3], Lugli S. [4], Manzi V. [1, 2], Montagna P. [5], Roveri M. [1, 2], Sierro F. J. [6], Taviani M. [5, 7, 8]

(1) Dipartimento di Fisica e Scienze della Terra, University of Parma, Parco Area delle Scienze, 157/A, 43100 Parma, Italy
(2) Alpine Laboratory of Paleomagnetism (ALP), Via Madonna dei Boschi 76, Peveragno 12016 (CN), Italy
(3) Laboratoire des Sciences du Climat et de l'Environnement (LSCE), Avenue de la Terrace, 91198, Gif-sur-Yvette, France
(4) Dipartimento di Scienze Chimiche e Geologiche, University of Modena and Reggio Emilia, via Campi 103, 41125 Modena, Italy
(5) Istituto di Scienze Marine (ISMAR-CNR), Via Gobetti 101, 40100 Bologna, Italy
(6) Department of Geology, University of Salamanca, 37008, Salamanca, Spain
(7) Biology Department, Woods Hole Oceanographic Institution, 266 Woods Hole Road, Woods Hole, MA 02543, USA.
(8) Stazione Zoologica Anton Dohrn, Villa Comunale, 80121 Naples, Italy.

* Corresponding author
Email: matteo.reghizzi@studenti.unipr.it

Abstract

The Sorbas basin is a reference sector of the Mediterranean basin for the definition of the onset of the Messinian salinity crisis straddling the transition from the open marine deposits (Abad marls) to the Primary Lower Gypsum (Yesares Formation) during the first stage of the crisis, between 5.97 and 5.60 Ma. Because of its proximity to the Atlantic gateway, the Sorbas basin is pivotal for the study of the oceanographic evolution that led to the most dramatic environmental event in the Mediterranean Sea. We measured the carbon ($\delta^{13}C$), oxygen ($\delta^{18}O$) and strontium ($^{87}Sr/^{86}Sr$) isotope ratio of 50 samples of planktonic foraminifera, mollusk shells, gypsum and carbonate sediments from the Abad and Yesares Members (Turre and Caños Formation) in the Perales, Hueli, Los Yesos and Rio de Aguas sections. Our results show a long-term trend with most of the values plotting within the range of the global ocean strontium isotope curve and distinct short-term fluctuations on precessional time scale. The investigated geochemical proxies suggest that these oscillations reflect significant input of continental waters into the basin during the humid phase of a single precessional cycle. This implies that the Western Mediterranean did not experience a main disconnection from the global ocean water before and during the first stage of the Messinian salinity crisis and that different Milankovitch forcings played a significant role in determining the seawater geochemistry.

Keywords: *Messinian salinity crisis, Mediterranean basin, Strontium isotopes, Oxygen and carbon stable isotopes, Sorbas basin, Spain, Paleoceanography.*

1. Introduction

The Messinian represents a crucial period for the evolution of the Mediterranean basin, which experienced major geological, hydrological and oceanographic changes with catastrophic consequences on its aquatic ecosystems. The study of these upheavals has not yet led to a full comprehension of the succession of events that occurred since about 6 Ma. One open question regards the timing and the modalities of the paleoceanographic changes occurring during the upper part of the pre-evaporitic phase up to the onset of evaporites precipitation (Roveri et al., 2014a). According to the three stages evolutionary model proposed by Roveri et al., 2014a (Fig. 1a), during the Messinian salinity crisis (MSC) the Mediterranean was affected by series of climate-induced environmental modifications characterized by the deposition of peculiar geological units in terms of paleoenvironmental, sedimentological and geochemical signatures (Müller and Mueller, 1991; Flecker et al., 2002; Flecker and Ellam, 2006; Roveri et al., 2014a, b). The MSC onset in the Mediterranean occurred synchronously at 5.971 Ma (Manzi et al., 2013), following the progressive restriction of the Mediterranean circulation and the establishment of water column stratification starting at 7.12 Ma (Kouwenhoven and van der Zwaan, 2006; Sierro et al., 2001). The latter is recorded basinwide by the cyclical and orbitally-controlled deposition of marls, diatomites and organic rich sediments in open marine settings in the Western (Abad Member, Sorbas basin; Sierro et al., 1999, 2001, Krijgsman et al., 2001), Central (Tripoli Formation., Caltanissetta basin; Bellanca et al., 2001; Blanc-Valleron et al., 2002) and Eastern Mediterranean (Pakhna Formation, Cyprus; Gavdos basin, Greece; Krijgsman et al., 1999a, 2002; Manzi et al., 2016).
The Sorbas basin (Betic cordillera, Spain, Fig. 1b) preserves a stratigraphically continuous transition between the pre-evaporitic open marine deposits (Abad marls; Sierro et al., 2001, 2003) and stage 1 evaporites (Yesares Formation; Lugli et al., 2010; Manzi et al., 2013). Thus, it represents a key area for understanding the Western Mediterranean paleoceanographic evolution during this crucial period of the Late Miocene history. The sedimentary succession of the Sorbas basin is characterized by a strong lithological cyclicity that has been interpreted as the result of astronomical-induced climatic variations, with arid conditions at insolation minima alternated to more humid situations at insolation maxima (Krijgsman et al., 2001; Sierro et al., 2001; Lugli et al., 2010; Manzi et al, 2013).
Here, we present the first high-resolution (precessional scale) isotope record (Sr, C, O) for the Western Mediterranean extending from the normal marine sediments up to the first stage of the salinity crisis (6.7 – 5.7 Ma). These data provide a substantial improvement of the Late Miocene geochemical database and allow to better understand the complex mechanisms that led to the onset of the MSC.

2. The importance of Sr isotopes for the paleoceanographic reconstruction

The global $^{87}Sr/^{86}Sr$ signature of the global oceanic water has changed significantly through the Earth's history and is considered a useful chronostratigraphic tool (McArthur et al., 2001; 2012). The $^{87}Sr/^{86}Sr$ signal of sediments may also provide clues for the comprehension of the oceanographic evolution of ancient basins (Elderfield, 1986). The oceanic mixing time is 1500 years on average and much shorter than the residence time of Sr, which spans several million years (Hodell et al., 1990; Topper et al., 2011), providing geochemical uniformity of the oceanic water with respect to Sr at a given time (Elderfield, 1986; Flecker and Ellam, 2006). On the other hand, in semi-enclosed basins, characterized by reduced exchanges with the global ocean, $^{87}Sr/^{86}Sr$ represents a highly sensitive tool to detect non-oceanic inputs, because freshwaters riverine discharge affects the Sr isotope signature (Roveri et al., 2014b, Topper et al., 2014). For these reasons, the Sr signal is pivotal for a better appreciation of the paleoceanographic evolution and hydrological budget of the Mediterranean and its sub-basins during the MSC.
An extensive $^{87}Sr/^{86}Sr$ database has been established for the Messinian onshore and offshore evaporitic deposits, over the past three decades (McCulloch and De Deckker, 1989; Müller et al., 1990; Müller and Mueller, 1991; Roveri et al, 2014b). The compiled data show that the Mediterranean $^{87}Sr/^{86}Sr$ values progressively diverged from the global ocean at the dawn of the MSC (Fig. 1c; Flecker et al., 2002, Flecker and Ellam., 2006, Topper et al., 2011, Roveri et al., 2014b). This change has been related to the progressive isolation of the Mediterranean Sea and the consequent gradual decrease of the oceanic input into the basin and/or to the increase of freshwater input from rivers (mainly Nile and Rhone; McArthur et al., 2001; Schildgen et al., 2014) and/or from the Paratethys (Flecker et al., 2002; Flecker and Ellam, 2006; Gladstone et al., 2007; Topper et al., 2011; Topper and Meijer, 2013; Roveri et al., 2014b, c). These factors allowed the development of a distinct Sr isotopic signature for the Mediterranean basin during the MSC, which significantly differs from the coeval global ocean signal. According to the revised version of the Sr isotope curve proposed by Roveri et

al. (2014b), the three phases of the crisis are characterized by well-defined non-overlapping $^{87}Sr/^{86}Sr$ ranges, with the maximum detachment from the oceanic signal (values decreasing to 0.708500) coinciding with the third stage (Upper Evaporites, Lago Mare) (Fig. 1c). The abrupt switch of the $^{87}Sr/^{86}Sr$ values to open marine conditions corresponds to the Messinian/Zanclean boundary, which marks the end of the crisis (McKenzie et al., 1988).

The most recent reconstruction of the $^{87}Sr/^{86}Sr$ curve for the period preceding the onset of the MSC was proposed by Flecker and Ellam (2006), integrating new measurements with literature data (Müller et al., 1990, Müller and Mueller, 1991, Montanari et al., 1997, Flecker and Ellam, 1999, Flecker et al., 2002, Sprovieri et al., 2004). Unfortunately, this dataset is somewhat biased because of the limited number of suitable sections for this exercise, which are never individually representative of the whole Mediterranean basin. A case in point is the lack of the Primary Lower Gypsum unit (PLG) at the onset of the MSC, like at the top of the Pissouri Motorway section (Cyprus; Manzi et al., 2016). Moreover, the value of the Sr record as a tool suffers additional weakness, such as the transition between the pre-evaporitic deposits and the first clear evidences of evaporitic conditions. This is exemplified by the questionable foraminifera material form the Ahmetler section, Southern Turkey (Flecker and Ellam, 1999), likely recycled from older units as suggested by an upward decreasing trend of the $^{87}Sr/^{86}Sr$ compared to the global ocean. These problems conspire to pinpoint straightforwardly the onset of the MSC and consequently to understand unequivocally the many paleoceanographic implications. The only section encompassing the early steps of the MSC is at Gavdos (Greece; Flecker et al., 2002), but unfortunately the succession does not contain evaporites. In addition, the uppermost pre-MSC deposits are only reported thus far in the Eastern Mediterranean, whereas data from the western region are missing. Due to its proximity to the Atlantic gateways, the western area should in principle better document the supposed gradual reduction of the oceanic influence into the Mediterranean basin, and any concurrent geochemical variations in the seawater structure. In our opinion the best candidate to study the transition is the astronomically calibrated succession of the Sorbas basin (Abad composite and Perales sections) because it includes a complete record from the pre-MSC deposits (Sierro et al., 2001, 2003) to the Primary Lower Gypsum (Lugli et al., 2010) that are correlated bed by bed with the other Mediterranean key sections (Manzi et al., 2013).

3. The Perales composite: a reference section for the Western Mediterranean

The Sorbas basin is a small Late Neogene depression that evolved in the Eastern Betics within a structural domain subjected to compressional and extensional events (Montenant and Ott d'Estevou, 1996). This area was part of the Betic Corridor which connected the Atlantic and the Mediterranean during the Late Miocene (Sierro et al., 1999, 2001) (Fig. 1b). The pre-evaporitic succession of the Sorbas basin is represented by the Turre Formation, starting with late Tortonian shallow marine calcarenitic deposits of the Azagador Member unconformably overlaying the middle-upper Tortonian turbidites of the Chozas Formation, or the Betic metamorphic basement (Völk and Rondeel, 1964; Sierro et al., 2001). These deposits rapidly grade upwards into the Abad Member consisting of bedded marls, opal-rich carbonate sediments, diatomites and sapropels of early Messinian age; this transition reflects a rapid deepening of the basin approximately at the Tortonian-Messinian boundary (Krijgsman et al., 2001). The Abad marls were deposited in the deep central portion of the Sorbas basin (Montenant and Ott d'Estevou, 1996; Martin and Braga, 1994) and provide a continuous stratigraphic record from the Tortonian-Messinian boundary (T/M; top of the Azagador Member, 7.246 Ma; Hilgen et al., 2012) to the base of the evaporites (Yesares Member), corresponding to the MSC-onset (5.971 Ma; Manzi et al., 2013). The Abad composite (Sierro et al., 2001) is a reference section for the Astronomical Polarity Time Scale because it is the only Messinian astronomically-tuned section providing reliable paleomagnetic data (Krijgsman et al., 1999a, 2001) and planktonic foraminifera biostratigraphy (Sierro et al., 2001). The succession includes up to 55 precessional cycles and is subdivided into two units: the Lower Abad (LA) and the Upper Abad (UA). The LA unit consists of 21 cycles given by the alternation of opal-rich indurated layers with homogeneous upper bathyal marls with fauna indicative of normal well-oxygenated open marine waters (Krijgsman et al., 2001). The UA starting at 6.7 Ma, consists of 34 quadripartite cycles with a sapropel layer, a lower homogeneous marl, a diatomite bed and an upper homogeneous marl. Very thin fine-grained sand and silt turbidites are locally intercalated within the sapropel suggesting a punctuated terrestrial input into the basin. The diatomite beds show a faint lamination at the base that become more evident in the upper part of the layer (Sierro et al., 1999, 2001, 2003). According to Sierro et al. (2001), the marls of the LA and the sapropels of the UA were deposited during insolation maxima. The onset of sapropel deposition at 6.7 Ma corresponds to a Mediterranean paleoceanographic event characterized by a reduction in the deep and intermediate water circulation (Blanc-Valleron et al., 2002; Kouwenhoven et al., 2006) leading to anoxic

seabottom conditions testified by the absence of benthic life. Moreover, changes in the planktonic foraminifer community since 6.7 Ma suggest climatic-forced variations in the hydrological conditions of the water column and in the nutrient abundance on different time scales (Sierro et al., 2003): i) at the precessional-scale, with the alternation of warm oligotrophic and cold eutrophic species (during insolation maxima and minima, respectively); ii) at both precessional and eccentricity-scale, with the increase and decrease of planktonic abundance (during maxima and minima, respectively). The last depositional cycles of the Abad composite can be directly correlated with the Perales section described by Manzi et al. (2013), which contains the onset of the MSC and is correlated with the other Mediterranean sections. The PLG unit is present in this area with up to 15 shale-marl/gypsum cycles including selenite facies associations which have been correlated across the Mediterranean (Lugli et al., 2010).
In this work we focused on a time interval of about 1 Myr (~6.70–5.70), including 47 precessional cycles: 34 in the Upper Abad and 13 in the Yesares Member (PLG unit, Lugli et al., 2010).

4. Materials and methods

A total of 50 samples were investigated for this study. In particular, 37 foraminifer, 5 mollusk and 8 evaporite (7 gypsum, 1 carbonate) samples were analyzed for strontium isotopes ($^{87}Sr/^{86}Sr$). Combined analyses of $\delta^{18}O$ and $\delta^{13}C$ and $^{87}Sr/^{86}Sr$ were performed on samples with enough material: 25 out of 37 foraminifer samples.
The foraminifer samples are sourced from the Perales C section, representing the uppermost part of the Abad composite (Sierro et al., 1999, 2001). Mollusk and evaporite samples were collected from other well-correlated sections nearby (Perales 37°5'56.53"N-2°3'14.36"O, Rio Aguas 37°5'6.50"N-2°6'51.45"O, Los Yesos 37°4'57.74"N-2°18'21.57"O and Hueli 37°4'45.25"N-2°6'56.15"O, Fig. 1b). The stratigraphic positions of the samples are reported on the Perales composite section (Fig. 2), compiled by merging the upper part of the Abad composite (Sierro et al., 2001) and the Perales section (Manzi et al., 2013). Furthermore, the stratigraphic position of samples from the stage 1 interval is conventionally reported on the Los Molinos section, which represents the entire PLG sequence of the Sorbas basin (Lugli et al., 2010) (Fig. 2). In order to test possible diagenetic modifications of the foraminifera we performed a screening and comparison among the poorly and well preserved tests under reflected light microscope and SEM. We checked the effects of the leaching procedure, described below, on internal and external features of foraminiferal shells of two samples (PER 2270 and MAB 5600) from the top-most portion of the UA.
After drying and weighing, rock samples were washed and sieved through 150 and 62 µm meshes. A total of 37 samples from the UA interval were selected from those previously analyzed for biostratigraphy and stable isotopes (Sierro et al., 1999, 2001, 2003). Samples were selected on the basis of neogloboquadrinid distribution along the UA interval, ~6.7-6.0 Ma. Whenever possible, we used only neogloboquadrinid specimens (*Neogloboquadrina acostaensis* and, occasionally, *Neogloboquadrina humerosa*), because of their nearly continuous distribution along the unit and their life habitat. In fact, these planktonic foraminifera display the highest abundance in stratified environments of the modern ocean, associated with high-productivity and deep chlorophyll maximum (DCM), where the nutricline and pycnocline are located above the base of the euphotic zone (Sierro et al., 2003). Neogloboquadrinids live at intermediate water depths less influenced by surface waters during the humid phase (Sierro et al., 2003) and therefore represent excellent geochemical archives to monitor the water column changes during an entire precessional cycle. For 7 out of 39 foraminiferal samples, the available neogloboquadrinids specimens were not abundant enough for Sr isotope analyses as they are almost totally absent during sapropel deposition, due to relatively warm winter temperatures (Sierro et al., 2003). In levels where neogloboquadrinids were not available in sufficient number (see Table 1), undifferentiated planktonic foraminifera (principally *Globigerina bulloides*, *Globigerinoides sacculifer*, *Turborotalita quinqueloba* and *Turborotalita multiloba*) were also picked. Several cross-check analyses performed on particularly abundant samples indicate that no isotopic fractionation occurs among sub-samples consisting only of neogloboquadrinids and sub-samples consisting of the other selected foraminifer assemblages (see discussion in Section 6.2). Only 8 of the UA cycles have not been investigated, due to the impossibility to obtain sufficient foraminifer tests for the isotope analyses (Fig. 2).

4.1. Sr isotope analyses

4.1.1. Foraminifer samples

$^{87}Sr/^{86}Sr$ of planktonic foraminifera has been measured in two different analytical sessions (28 samples during June 2014; 9 samples during August 2015). At least 100 planktonic foraminifer tests (~ 1 mg) were hand-picked from the >150 µm fraction. Shells affected by obvious calcite overgrowths on the external and/or inner surface were preventively excluded. Samples were ultrasonically washed in MilliQ water for 10 min to remove residual particles and leached with 0.01M HCl in order to dissolve possible carbonate contaminants, such as the coccolith fraction that may alter the original isotopic composition, as described by Reinhardt et al. (2000). The samples were subsequently dissolved in 0.5 mL of 5M acetic acid to minimize the concomitant dissolution of any siliciclastic contaminants. The solutions were centrifuged to remove the insoluble residue, evaporated to dryness and reacidified in 3 mL of 3M HNO_3. Strontium was isolated from the carbonate matrix using Eichrom Sr-SPEC resin, following the method reported in Palmiotto et al. (2013). Final solutions were adjusted to a concentration of 4% w/w HNO_3 and analyzed within a few days. Strontium isotope ratios were obtained using a multi collector inductively coupled plasma mass spectrometer (HR-MC-ICPMS Thermo Scientific™ Neptune), housed at CIGS (Centro Interdipartimentale Grandi Strumenti, University of Modena and Reggio Emilia). Strontium concentration was previously tested by using a quadrupole inductively coupled plasma mass spectrometer (ICPMS X Series II, Thermo Fisher Scientific). Sample solutions were then diluted to 35 ppb and introduced into the Neptune via a high sensitivity desolvating inlet system ESI-APEX IR and a 100 µL/min nebulizer. The sensitivity for 35 ppb Sr was 14 V on the ^{88}Sr peak and the blank level (4% w/w HNO_3) was < 0.03 V. The strontium isotope standard NIST SRM 987, with a generally accepted $^{87}Sr/^{86}Sr$ value of 0.71026 ± 0.00002 (Ehrlich et al., 2001) has been used as an external standard. Samples, standards and blank solutions were analyzed in a static multi-collection mode in a single block of 100 cycles with an integration time of 8.389 s per cycle. Samples were analyzed using a bracketing sequence (blank/standard/blank/sample/blank) in order to correct for any instrumental drifts. The $^{87}Sr/^{86}Sr$ ratios were corrected for mass fractionation (mass bias) effect using $^{88}Sr/^{86}Sr$ = 8.37520 as normalizing ratio and an exponential law. Isobaric interferences of ^{86}Kr and ^{87}Rb on ^{86}Sr and ^{87}Sr species respectively were also considered. Finally, values obtained for the NIST SRM 987 standard measured before and after each sample in the bracketing sequence were used for C-factor calculation ("C-factor" = true isotope ratio (i.e. 0.71026) divided by the average value of the two standards measured). Each sample's isotope ratio has been multiplied by the obtained C-factor value in order to be corrected by a possible instrumental drift. Repeated measurements of the NIST SRM 987 standard yielded a mean value of 0.710279 ± 0.000013 (2 S.D., n = 30) in June 2014, and 0.710260 ± 0.000009 (2 S.D., n = 11) in August 2015. For both analytical sessions, the internal precision on individual standard analysis varied between 0.000005 and 0.000008 (2 S.E.). For all samples the instrument gave an average internal uncertainty value of 0.000009 (2 S.E.), with a minimum value of 0.000006 and a maximum of 0.000022.

4.1.2. Evaporite samples

Evaporite samples were analyzed at SUERC (Scottish Universities Environmental Research Centre, East Kilbride, Scotland) and prepared for $^{87}Sr/^{86}Sr$ determination following the procedure described in Roveri et al. (2014b). Primary selenite crystals and the carbonate sample were crushed using a hand-mortar. Powdered samples were leached in 1M ammonium acetate prior to acid digestion with HNO_3. Sr was separated using Eichrom Sr SPEC resin. Matrix elements were eluted in 8M HNO_3 before elution of Sr in 0.01M HNO_3. In preparation for mass spectrometry, Sr samples were loaded onto single Re filaments with a Ta-activator. Sr samples were analyzed with a VG Sector 54-30 multi collector thermal ionization mass spectrometer. A ^{88}Sr intensity of 1 V ± 10% was maintained. The instrumental mass fractionation was corrected by using a stable isotopic $^{86}Sr/^{88}Sr$ ratio of 0.1194 and an exponential law. The mass spectrometer was operated in the peak-jumping mode with data collected as 15 blocks of 10 ratios, which gives an internal uncertainty of < 0.000020 (2 S.E.). Repeated measurements of the strontium isotope standard NIST SRM 987 gave 0.710249 ± 0.000016 (2 S.D., n = 17) during this session of analysis. The internal precision on individual analyses was between 0.000014 and 0.000020 (2 S.E.).

4.1.3. Mollusk samples

The mollusk samples consist of calcitic bivalves, i.e. ostreid fragments, except for sample H2, which consists of a pectinid shell. Three samples were analyzed at the Laboratoire des Sciences du Climat et de l'Environnement (France) in March 2013. $^{87}Sr/^{86}Sr$ was obtained from small shell fragments (~ 15 mg), mechanically cleaned using a small diamond cutting disc attached to a handheld dental drill in order to remove

all visible contaminations and sediment-filled cavities. They were subsequently crushed into small chunks (ca. 1-2 mm in size) in a hand-mortar and examined under a binocular microscope. Any further contamination was removed by hand-picking. The pieces of carbonate were chemically cleaned following the procedure published by Li et al. (2011), which involves sequential leaching steps with acetic acid. The final supernatant solution was completely evaporated and adjusted to 3M HNO_3 for ion exchange chromatography. Strontium was isolated from the carbonate matrix using Eichrom Sr-SPEC resin, following the method reported in Palmiotto et al. (2013). Strontium isotope ratios were measured using a Thermo Scientific™ Neptune^{Plus} multi collector ICPMS. The solution was diluted to 60 ppb of Sr and introduced into the mass spectrometer using an ESI-APEX desolvating system and a 100 µL/min nebulizer. The sensitivity for 60 ppb was about 12 V on ^{88}Sr peak and the chemical blank level (0.5M HNO_3) was < 0.02 V. The instrumental mass fractionation was corrected by using a stable isotopic ^{86}Sr/^{88}Sr ratio of 0.1194 and an exponential law. Only minor corrections for ^{87}Rb on ^{87}Sr and ^{86}Kr on ^{86}Sr were considered and no isobaric corrections for Ca dimers and argides were required. Repeated measurements of the strontium isotope standard NIST SRM 987 during the analytical session yielded a mean ^{87}Sr/^{86}Sr value of 0.710018 ± 0.000015 (2 S.D., n = 7). The solutions of the three samples were analyzed twice (20-21 March 2013) and the results reported in Table 1 represent the average values of the two analytical sessions. Two mollusk samples were analyzed at CIGS (University of Modena and Reggio Emilia) in July 2016, following the procedure for sample preparation, Sr extraction and analysis described above. The sensitivity for 200 ppb Sr was 8 V on the ^{88}Sr peak and the blank level (4% w/w HNO_3) was < 0.01 V. Repeated measurements of the NIST SRM 987 standard yielded a mean value of 0.710262 ± 0.000015 (2 S.D., n = 12) during this analytical session. The average internal uncertainty on individual analyses was 0.000010 (2 S.E.), with values between 0.000009 and 0.000013.

4.2. Carbon and oxygen isotope analyses on foraminifera

A total amount of 30 foraminifera specimens were selected, ultrasonically cleaned in MilliQ water and leached with a 0.01M HCl solution using the same procedure described for the Sr analyses. Samples were analyzed on a ThermoFinnigan GasBench II equipped with a CTC Combi-Pal autosampler linked to a ThermoFinnigan Delta^{Plus} XP isotope ratio mass spectrometer, housed at the Parma Isotope Geochemistry Lab (University of Parma). Carbonate isotope ratios (^{18}O/^{16}O and ^{13}C/^{12}C) are reported as δ^{18}O and δ^{13}C per mil relative to Vienna Pee Dee Belemnite (VPDB) by assigning a δ^{13}C value of +1.95‰ and a δ^{18}O value of -2.20‰ to NBS 19. The overall external analytical precision based on replicate analysis of laboratory standards was better than ± 0.23 ‰ for δ^{18}O and ± 0.10 ‰ for δ^{13}C.

5. Results

5.1. ^{87}Sr/^{86}Sr from pre-MSC sediments and stage 1 evaporites (6.70–5.70 Ma)

Most of the ^{87}Sr/^{86}Sr values from both pre-evaporitic period (foraminifera) and first stage of the MSC (evaporites) plot within the range of the global ocean curve and show a gently increasing trend comparable to Late Miocene oceanic values (from 0.708940 to 0.709020 ± 0.000025 for the Messinian, 7.246–5.333 Ma), with no clear evidence of a major detachment from the coeval global oceanic Sr curve (Fig. 3). Regarding the mollusks, one sample shows a ^{87}Sr/^{86}Sr value clearly above the coeval oceanic range (0.709071), while the others plot within the range of the PLG unit (Roveri et al., 2014b). Four foraminifer samples of the lowermost portion of the UA section (>6.5 Ma; i.e. before cycle UA10), show values plotting far above the coeval oceanic range (up to 0.709250; Fig. 4a). The sapropel and marl intervals belonging to the same precessional cycles in the pre-MSC unit show a clear diversification in ^{87}Sr/^{86}Sr, with values within the oceanic curve for the marl and systematically negative excursions for the sapropel, especially for the interval between UA18 and UA21, where we have the best sampling resolution.

5.2. δ^{18}O and δ^{13}C data from pre-MSC deposits (6.70–6.00 Ma)

Neogloboquadrinid-derived δ^{18}O and δ^{13}C data from the UA show a rather linear trend for most of the interval considered, with values ranging from -4.6‰ to +2.3‰ and from -4.6‰ to -1.0‰ for oxygen and carbon, respectively. Oxygen isotope record shows more negative (or ^{18}O depleted) values and an increasing amplitude of variability with a range from -4.6‰ to +1.0‰, above cycle UA27. The δ^{13}C values also shows a (less evident) trend slightly towards more negative values seven cycles below the MSC inception (Fig. 5).

6. Reliability of the isotopic values from the Upper Abad interval

6.1. $^{87}Sr/^{86}Sr$ before 6.5 Ma

Four samples from the lowermost part of the UA section show values that are much higher than the coeval Sr oceanic signature (Fig. 4a) suggesting the presence of radiogenic Sr input into the basin around the LA-UA transition (~6.7 Ma). A possible proxy to detect this effect could be the measure of the terrigenous input in the Abad marls using the weight percent of the sand-sized residue (> 150 μm) remained after the washing and sieving procedure for biostratigraphic analyses. In this interval, the sand percentage reaches up to 25% of the whole rock, then slowly decreases and remains constant up to the top of the Abad unit, with contents four times lower than before (Fig. 4a). This does not mean that the input of the radiogenic Sr is directly proportional to the amount of sand in the basin, but simply that the presence of terrigenous sediments could explain the high radiogenic Sr in the water mass. The occurrence of chaotic sedimentary bodies (slump) and the presence of ash layers in the LA up to the first cycle of UA (Sierro et al., 2001) could testify the tectonic uplift of the basin margin during the pre-MSC (Mather et al., 2001) and could have favored the delivery of external Sr sources into the basin likely derived from the recycling of the surrounding volcanic rocks and the Betic metamorphic basement. These rocks are a potential source of radiogenic Sr, as testified by the high $^{87}Sr/^{86}Sr$ values (up to 0.714390) of the coeval volcanic complex of Cabo de Gata (Duggen et al., 2004). Water geochemistry of a small and marginal basin like Sorbas could very likely reflect these recycling effects. For these reasons, this anomalous cluster of samples, likely affected by an external agent that has distorted the primary $^{87}Sr/^{86}Sr$ values of calcareous foraminifera analyzed, will not be considered in the discussion.

6.2. $^{87}Sr/^{86}Sr$ on different foraminifer assemblages

Sr isotopic composition of 7 out of 37 foraminiferal samples is the result of diverse planktonic foraminifer taxa and not only neogloboquadrinids. We performed five replicates of a single sample (MAB5600, lower homogeneous marls of cycle UA30), chosen because of abundance of both planktonic and benthic foraminifera. $^{87}Sr/^{86}Sr$ was tested on a sub-sample consisting of only neogloboquadrinid specimens, on two sub-samples consisting of other planktonic species and two more sub-samples consisting of only benthic species (Fig. 4b, c). The results provide two main outcomes: i) a clear diversification in $^{87}Sr/^{86}Sr$ signal between planktonic and benthic species, with planktonic species showing values consistent within the coeval oceanic range and benthic providing consistently lower values; ii) no substantial differences between samples constituted by mixed planktonic foraminifera and those solely including neogloboquadrinids, with $^{87}Sr/^{86}Sr$ values of each samples plotting between their half uncertainty range. This validates our decision to exclude the benthic foraminifera from our study, in order to avoid any modification of the Sr signal influenced by particular (inhomogeneous) water conditions. The differences between planktonic and benthic foraminifera's $^{87}Sr/^{86}Sr$ values could indicate that the reprisal of deep water ventilation starting with the deposition of the lower homogeneous marls (Sierro et al., 2003) was unable to produce a homogeneous Sr signal throughout the water column. Thus, this signal is probably not fully representative of undisturbed and homogeneous water column conditions. Furthermore, we can consider the $^{87}Sr/^{86}Sr$ signal of those samples for which both neogloboquadrinids and other planktonic foraminifera were selected as reliable.

6.3. Preservation of foraminifera

While most of the foraminiferal tests below UA27 appeared well preserved, specimens from the uppermost part of the section proved to be frequently affected by euhedral calcite overgrowths on the outer shell surface, and sporadically by sparry calcite infilling. The higher variability in stable isotope composition and a shift to more negative values detected in this younger interval, called for checking the potential contamination of original signals by secondary cements and/or allochtonous material (Fig. 5).
External and internal features of foraminiferal tests have been investigated by means of SEM images before and after the leaching process described in Section 4.1.1. (Fig. 6). Tests representing various degrees of preservation from worst to best, have been inspected to appreciate the effects of the leaching process. As a first step, all samples showing abundant calcite overgrowths, as the unleached PER 2270 sample (Fig. 6a), were discarded. We checked the effects of the leaching procedure that we applied to all samples (see Section 4.1.1)

and the presence of non-primary features in the foraminifer tests of samples PER 2270 and MAB 5600, both from the top-most portion of the UA. Sample PER2270 shows a bad preservation and a more negative stable isotope composition with respect to sample MAB 5600. Unleached PER 2270 sample (Fig. 6a, e, i) shows abundant marl incrustations and calcite overgrowths on the external surface and a carbonate infill, but no signs of recrystallization are visible in the inner texture of the shell. In contrast, the unleached foraminifer tests picked in sample MAB 5600 (Fig. 6c, g, m) is well preserved and thought as representative of the majority of the analyzed samples. The leaching process provides a significant cleaning of the outer surface and inner part of foraminifera, even in cases of initially compromised conditions (Fig. 6b, f, l - leached sample PER 2270; Fig. 6d, h, n - leached sample MAB 5600) and a complete removal of the calcareous nannofossil contamination observed in a few samples. We also observed that the leaching does indeed effectively remove the material trapped within the pores of the foraminifer shells. Ultrasonication ensures the fragmentation of shells and an efficient detachment of the secondary calcite rims and infills, which are either dissolved by the subsequent weak HCl leaching or mechanically removed by centrifugation. These observations allow us to consider the leaching procedure not only useful, but necessary to ensure a high reliability of the geochemical values. Furthermore, the well preserved, microgranular internal structure of the foraminifer walls, also visible in the badly preserved specimens (sample PER2270), allows us to consider reliable the stable isotopic results related to foraminifer from the top-most part of the UA interval.

6.4 . $^{87}Sr/^{86}Sr$ of mollusk shells

In the absence of foraminifera after the beginning of the MSC, the only available Sr signal for the stage 1 can be obtained from the primary evaporites, which were deposited during the insolation minima (Roveri et al., 2014b). However, shale interbedded within the PLG beds in the Sorbas basin contain mollusk, which offers a unique opportunity to define the geochemical conditions when the sapropels were depositing at insolation maxima. With one exception, mollusks show values that detach from the global ocean curve, but are still within the $^{87}Sr/^{86}Sr$ range of stage 1 (Roveri et al., 2014b). The lower values measured in the mollusks with respect to stage 1 PLG (this work), resemble the difference showed by the pre-MSC foraminifera in the sapropel rather than in the marls (discussed in the following paragraph). While useful to shed light on the variations between arid and humid hemicycles, mollusk and evaporite samples are still too few to provide information about possible precessional-scale oscillations. However, these values represent the first data available from the insolation maxima during gypsum deposition.

7. Short- to long-term geochemical oscillations

The general trend of $^{87}Sr/^{86}Sr$ values does not suggest a strong modification of Sr geochemistry of the Sorbas basin compared to the open ocean signal (Fig. 3). The values remain generally within or close to the global oceanic curve for the entire time interval, with no clear deviation. This suggests that the Sorbas basin did not experience a significant detachment from the global ocean and was still efficiently influenced by oceanic water before the MSC onset and during the transition to evaporative conditions of stage 1. At a smaller scale, the isotope values reveal two main oscillation trends, discussed below: i) a shorter-term variability, related to the arid-humid climate oscillations controlled by precessional forcings; ii) a longer-term variability controlled by the 400-kyr eccentricity.

7.1. Short-term oscillations (precessional scale)

The sampling resolution (in some cases more than two samples for a single UA cycle, Fig. 2) allowed us to reconstruct the climate-driven hydrological changes within a single precessional cycle. At times of summer insolation minima, i.e. the arid phase of the insolation cycle, the water column was characterized by efficient vertical mixing and deep-water ventilation. This was favored by lower winter temperatures and higher surface water salinity, due to scarce annual rainfall and weak continental riverine input (Sierro et al., 2003). A weak fresh water supply is reflected in the foraminifer carbonate geochemistry, which maintains a Sr isotope ratio characteristic of coeval oceanic water. Instead, seawater geochemistry during summer insolation maxima was affected by enhanced river discharge and higher annual precipitations. This increased the vertical density contrast into the basin, favoring the formation of a persistent pycnocline at depth and, consequently, a strong water column stratification (Sierro et al., 2003). It follows that during the humid phase of the cycle the influence of lower Sr isotope ratio provided by freshwater has been recorded by planktonic foraminifera. A

significantly higher input of continental water, probably Nile and/or Rhone derived (Keogh and Butler; 1999; Flecker and Ellam, 2006), occurred during the humid phase of the cycle, contributing to a general $^{87}Sr/^{86}Sr$ decrease, recorded by the foraminifer associations in the sapropel intervals. The semi-enclosed nature and the limited geographical extension of the basin probably amplified these short-term oscillations, due to the higher contribution of freshwater and faster water mixing process leading to Sr re-homogenization. The shorter-term climatic variability deduced from Sr isotope ratio oscillations, strongly influenced the deposition of different types of sediments of the UA unit, but did not cause an irreversible modification of the water geochemistry of the basin. In fact, after the decrease observed in the sapropel intervals, Sr isotope values are very similar to those of the global ocean during the marl deposition, confirming a persistent strong contribution of ocean water, which in turn suggests stable connections between the basin and the global ocean. Stable isotope data clearly reflect the different physical conditions of the water column during the two distinct climatic phases of a single precessional cycle, confirming an orbital control on the hydrological features of the Sorbas basin. Data related to the UA18-21 interval show an oscillating trend of carbon and oxygen isotopes, with clear variations from sapropel to marl depositions that can be easily linked to the Sr isotope variations (Fig. 7a). Lowest values of planktonic $\delta^{18}O$ occurred during Northern hemisphere (NH) summer insolation maxima and they are indicative of strong freshwater supply into the basin compared to the annual evaporation rate and a consequent decrease in surface water salinity. All these factors favored the stratification of the water column and prevented deep water convection and oxygen supply to the bottom, with the subsequent deposition of sapropels. The lack of vertical mixing, which usually occurs in winter and carries cold water to the surface, contributed to maintain warm-water at the surface that further decreased the $\delta^{18}O$ of the planktonic foraminifera. On the other hand, the marly intervals are systematically characterized by higher $\delta^{18}O$ values, indicative of more negative Mediterranean hydrologic budgets (i.e. weakly evaporative conditions). This suggests higher surface water salinity due to the freshwater deficit in response to more arid conditions that favored water mixing and led to deposition of marls during the insolation minima. Cooling of surface waters as reflected in the planktonic foraminifer assemblages (Sierro et al. 2003) due to upward mixing of deeper and colder water also contributed to the heavier oxygen isotopes of the planktonic foraminifera at insolation minima. Planktonic foraminifer $\delta^{13}C$ values in the sapropels are systematically higher than those found in the homogeneous marls. The $\delta^{13}C$ of dissolved inorganic carbon (DIC) in surface water is the result of isotope fractionation during air-sea exchange of CO_2 and the balance between the rate of production of organic carbon through photosynthesis and the remineralization rate of organic carbon (Lynch-Stieglitz et al., 1995; Zeebe and Wolf-Gladrow, 2001). Photosynthesis preferentially removes nutrients and ^{12}C, resulting in ^{13}C-enriched DIC of surface waters (Lynch-Stieglitz et al., 1995; Pierre et al., 1994, Pierre, 1999; Zeebe and Wolf-Gladrow, 2001). In contrast, the release of ^{12}C during remineralization of organic matter decreased the $\delta^{13}C$ of seawater DIC at depth. The heavier planktonic $\delta^{13}C$ values during sapropel deposition are unambiguously linked to prolonged periods of strong stratification of the water column and total nutrient consumption. The nutrient uptake by the phytoplankton at surface with a preferential removal of ^{12}C, which was transferred to the bottom, resulted in a pronounced increase in the $\delta^{13}C$ of surface waters. These typically high $\delta^{13}C$ values are observed today in the central part of the subtropical gyres with strong water stratification and surface waters completely devoid of nutrients, even though air-sea exchange would tend to lower the $\delta^{13}C$ of seawater DIC (Lynch-Stieglitz et al., 1995). The absence of vertical mixing of the water column at NH summer insolation maxima prevented the upward return of ^{12}C and nutrients to the surface and generated water anoxia at the bottom. Only when vertical mixing starts again at insolation minima, nutrients and ^{12}C are transported back to the surface, resulting in lower planktonic $\delta^{13}C$ values during the deposition of the homogeneous marls. Precessional-scale oscillations of $^{87}Sr/^{86}Sr$ and C and O stable isotopes strongly support the assumptions on the planktonic community's ecological response to astronomically induced climate variability (Sierro et al., 2003), confirming a climatic control on physical and hydrological conditions as well as the geochemical properties of the water.

7.2. Long-term oscillations (400 kyr eccentricity scale)

Another interesting result of this study is the long-term trend of $^{87}Sr/^{86}Sr$ values, superimposed on the shorter-term oscillations, that seems to fluctuate with a period of 400 kyr (Fig. 7b). By correlating all the insolation minima values (i.e. pre-evaporitic values from the marly intervals and the MSC values from the primary gypsum) it is possible to notice a trend that can be linked to the long (400 kyr) eccentricity frequency band. Unfortunately, the limited number of data available for the stage 1 interval prevents a clear identification of the trend, albeit it seems to persist across the onset at least for the first five gypsum beds. Sprovieri et al. (2004) already noticed a 400 kyr $^{87}Sr/^{86}Sr$ trend in the Late Miocene (Tortonian) sequence exposed in the Gibliscemi

section (Sicily, Hilgen et al., 1995). They showed that the influence of the Milankovitch cyclicity on the Sr isotope curve could be induced by periodic variations of riverine inputs. Hence, the combined effect of periodic fluctuations (increasing-decreasing) of continental runoff, induced by Milankovitch forcing, and the restricted setting of the basin, could have played a significant role in water Sr geochemistry variations also for the Sorbas basin, confirming an orbitally-driven climatic control on the late Miocene Mediterranean isotope oscillations.
The C and O stable isotope trends along the UA unit do not show oscillations that can be correlated with the $^{87}Sr/^{86}Sr$ long-term trend. The neogloboquadrinid $\delta^{18}O$ record fits well those of Sierro et al (2003) for *Globigerina bulloides* and *Orbulina universa*. Conversely, the $\delta^{13}C$ shows a distinctive general trend, characterized by intermediate values respect to the two other foraminifer taxa (Fig. 5) that probably reflects the different disequilibrium values of the three species. While *O. universa* shows a very small negative disequilibrium effect, *Neogloboquadrina* and *G. bulloides* exhibit very negative offsets from equilibrium $\delta^{13}C$ (Bemis et al., 2000; Birch et al., 2013). The neogloboquadrinid $\delta^{13}C$ also agrees with the one from *Globigerinoides obliquus* from the Metochia section (Kouwenhoven and van der Zwaan, 2006). Although we consider diagenetic modification unlikely (Fig. 6), it is not easy to interpret the increasing variability in the uppermost seven cycles of the UA interval (UA27-UA34; i.e. above ~ 6.12 Ma), because no reliable stable isotope data exist for other sections of the Mediterranean covering the same time interval. In particular, the stable isotopes record of Sierro et al. (2003) does not show the uppermost part above 6.25 Ma (cycle UA22), where we obtained scattered values. Kouwenhoven and van der Zwaan, (2006) as well do not report values from the uppermost interval. Blanc Valleron (2002) studied the Tripoli Formation in the Falconara section (Sicily) up to the first bed of the Calcare di base, but in this case the stable isotopes data were from bulk carbonate samples and cannot be compared with our data. The variability of $\delta^{18}O$ in the uppermost part of the section could be related to an increased amplitude of the physico-chemical oscillations of the water column approaching the crisis onset. The planktonic foraminifer assemblages reflect a more stressed environment, testified by the increasing proliferation of more opportunistic species adapted to a wide range of environmental conditions (e.g. salinity variation; Kroon et al., 1988), like *T. quinqueloba* and *T. multiloba*, from 6.40 to 6.06 Ma (cycles UA 15 to 31; Sierro et al., 2003). Stressed environmental conditions are also indicated by the highly fluctuating diversity and abundance of planktonic species from around 6.10 Ma to the MSC onset. Our preservation screening of foraminiferal test indicates that a diagenetic influence on isotopic results is unlikely (Fig. 6). Therefore, unlike the precessional-scale oscillations, which are recorded in the geochemical proxies, it is not possible to unambiguously interpret the long-term trend of stable isotopes for the upper part of the section. These long-term oscillations are similar to the climatic orbital cyclicities observed in the Atlantic Ocean for the late Neogene, recognized by the $\delta^{18}O$ and $\delta^{13}C$ trends of benthic foraminifera for two partially overlapping time intervals: 5 to 14 Ma in ODP site 926 (Shackelton and Hall, 1997) and 4.5 to 7 Ma in sites 999 and 1006 (Bickert et al., 2004).
As a general comment, it would be advisable to refer to curves detailing the same chronological interval, rather than to smoothed or averaged curves, like that of Mc Arthur (2001), to evaluate in a more accurate way the short- and long-term effects related to the variability of Earth orbital parameters. At present, one of the best references is the curve provided for the Indian Ocean (Farrell et al., 1995), although a high-resolution curve for the Northern Atlantic, at present still unavailable, would obviously be preferable.
Finally, our results suggest to expand this integrated isotope approach to other suitable areas of the Mediterranean region. This could bring to a better understanding of the paleohydrological and paleoceanographic changes that preconditioned the Mediterranean Sea for the salinity crisis.

8. Conclusions

The dataset obtained from the Sorbas basin represents the first complete Sr isotope stratigraphy for the Western Mediterranean straddling the salinity crisis onset contributes to reconstruct a reliable Mediterranean $^{87}Sr/^{86}Sr$ curve for the Late Miocene.
It highlights the high potential of the Sorbas basin to record oscillations of the water Sr, C and O isotopic signature on orbital time scales, before and during the MSC.
Between 6.50 and 6.00 Ma the $^{87}Sr/^{86}Sr$ and stable isotopes fluctuations suggest an important role of Milankovitch forcings in controlling the water geochemistry of small marginal basins with two distinct variabilities: i) a short-term one, which was precessionally-driven and ii) a long-term one (400 kyr) forced by eccentricity.
From the pre-MSC up to the first stage of the MSC, the Western Mediterranean was punctuated by cyclical dilution phases during humid hemicycles (insolation maxima), but it never experienced a full isolation from

the global ocean, as suggested by the alignment of the Mediterranean Sr isotope values with the global ocean $^{87}Sr/^{86}Sr$ curve.

Acknowledgments

Enrico Maria Selmo (University of Parma, Italy) and Rob Ellam (Scottish Universities Environmental Research Centre, East Kilbride, Scotland) are greatly acknowledged for the laboratory support for stable isotopes and for Sr isotope analyses on evaporites samples respectively. Patrick Grunert, Charlotte Schreiber, two anonymous reviewers and Isabel Patricia Montanez (Editor) are acknowledged for their constructive comments and suggestions that contributed to improve the manuscript. The Authors acknowledge the Fondazione Cassa di Risparmio di Modena for the financial support of the analytical facilities at the Centro Interdipartimentale Grandi Strumenti of the University of Modena and Reggio Emilia. This is ISMAR_CNR Bologna scientific contribution n° 1896.

References

Bellanca, A., Caruso, A., Ferruzza, R., Neri, R., Rouchy, J.M., Sprovieri, M., Blanc-Valleron, M.M., 2001. Transition from marine to hypersaline conditions in the Messinian Tripoli Formation from the marginal areas of the central Sicilian Basin. Sedimentary Geology 140, 87-105.

Bemis, B. E., Spero, H. J., Lea, D. W., and Bijma, J., 2000. Temperature influence on the carbon isotopic composition of *Globigerina bulloides* and *Orbulina universa* (planktonic foraminifera). Marine Micropaleontology, 38, 213–228.

Bickert, T., Haug, G.H., Tiedemann, R., 2004. Late Neogene benthic stable isotope record of Ocean Drilling Program Site 999: Implications for Caribbean paleoceanography, organic carbon burial, and the Messinian Salinity Crisis. Paleoceanography 19, PA1023.

Birch, H., Coxall, H. K., Pearson, P. N., Kroon, D., O'Regan, M., 2013. Planktonic foraminifera stable isotopes and water column structure: disentangling ecological signals. Marine Micropaleontology, 101, 127-145.

Blanc-Valleron, M.M., Pierre, C., Caulet, J.P., Caruso, A., Rouchy, J.M., Cespuglio, G., Sprovieri, R., Pestrea, S., Di Stefano, E., 2002. Sedimentary, stable isotope and micropaleontological records of paleoceanographic change in the Messinian Tripoli Formation (Sicily, Italy). Palaeogeography, Palaeoclimatology, Palaeoecology 185, 255–286.

Duggen, S., Hoernle, K., van der Bogaard, P., Harris, C., 2004. Magmatic evolution of the Alboran region: The role of subuction in forming the Western Mediterranean and Causing the Messinian Salinity Crisis. Earth and Planetary Science Letters 218, 91-108.

Ehrlich, S., Gavrieli, I., Dor, L., Halicz, L., 2001. Direct high-precision measurements of the $^{87}Sr/^{86}Sr$ isotope ratio in natural water, carbonates and related materials by multiple collector inductively coupled plasma mass spectrometry (MC-ICP-MS). Journal of Analytical Atomic Spectrometry 16, 1389-1392.

Elderfield, H., 1986. Strontium Isotope Stratigraphy. Palaeogeography, Palaeoclimatology, Palaeoecology 57, 71-90.

Farrell, J.W., Clemens, S.C., Gromet, L.P., 1995. Improved chronostratigraphic reference curve of late Neogene seawater $^{87}Sr/^{86}Sr$. Geology 23, 403-406.

Flecker, R., Ellam, R.M., 1999. Distinguishing climatic and tectonic signals in the sedimentary succession of marginal basin using Sr isotopes: an example from the Messinian salinity crisis, Eastern Mediterranean. Journal of the Geological Society, London 156, 847-854.

Flecker, R., de Villiers, S., Ellam, R.M., 2002.Modelling the effect of evaporation on the salinity–$^{87}Sr/^{86}Sr$ relationship in modern and ancient marginal-marine systems: the Mediterranean Messinian Salinity Crisis. Earth and Planetary Science Letters 203, 221–233.

Flecker, R., Ellam, R.M., 2006. Identifying Late Miocene episodes of connection and isolation in the Mediterranean–Paratethyan realm using Sr isotopes. Sedimentary Geology 188–189, 189–203.

Gladstone, R., Flecker, R., Valdes, P., Lunt, D., Markwick, P., 2007. The Mediterranean hydrologic budget from a Late Miocene global climate simulation. Palaeogeography, Palaeoclimatology, Palaeoecology 251, 254–267.

Hilgen, F.J., Lourens, L.J., Van Dam, J.A., 2012. The Neogene Period. In: Gradstein, F.M., Ogg, J.G., Schmitz, M.D., Ogg, G.M., (Eds.), The Geological Time Scale 2012. Elsevier B.V., Oxford, pp. 923-978.

Hilgen, F.J., Krijgsman, W., Langereis, C.G., Lourens, L.J., Santarelli, A., Zachariasse, W.J., 1995. Extending the astronomical (polarity) time scale into the Miocene. Earth and Planetary Science Letters 136, 495-510.

Hodell, D., Mead, G., Mueller, P., 1990. Variation in the strontium isotopic composition of seawater (8 Ma to present): Implications for chemical weathering rates and dissolved fluxes to the oceans. Chemical Geology 80, 291‑307.

Keogh, S.M., Butler, R.W.H., 1999. The Mediterranean water body in the late Messinian: interpreting the record from marginal basins on Sicily. Journal of the Geological Society, London 156, 837-846.

Kouwenhoven, T.J. van der Zwaan, G.J., 2006. A reconstruction of late Miocene Mediterranean circulation patterns using benthic foraminifera. Palaeogeography, Palaeoclimatology, Palaeoecology 238, 373-385.

Krijgsman, W., Hilgen, F.J., Raffi, I., Sierro, F.J., Wilson, D.S., 1999a. Chronology, causes, and progression of the Messinian salinity crisis. Nature 400, 652–655.

Krijgsman, W., Fortuin, A.R., Hilgen, F.J., Sierro, F.J., 2001. Astrochronology for the Messinian Sorbas basin (SE Spain) and orbital (precessional) forcing for evaporite cyclicity. Sedimentary Geology 140, 43–60.

Krijgsman, W., Blanc-Valleron, M.M., Flecker, R., Hilgen, F.J., Kouwenhoven, T.J., Orszag-Sperber, F., Rouchy, J.M., 2002. The onset of the Messinian salinity crisis in the Eastern Mediterranean (Pissouri Basin, Cyprus). Earth and Planetary Science Letters 194, 299–310.

Kroon, D., Wouters, P.F., Moodley, L., Ganssen, G., Troelstra, S.R., 1988. Phenotypic variation of Turborotalita quinqueloba (Natland) tests in living populations and in the Pleistocene of an Eastern Mediterranean piston core. In: Brummer, G.J.A., Kroon, D. (Eds.), Planktonic Foraminifers as Tracers of Ocean–Climate History. Free University Press, Amsterdam, pp. 131–147.

Laskar, J., Fienga, A., Gastineau, M., Manche, H., 2011. La2010: a new orbital solution for the long-term motion of the Earth. Astronomy and Astrophysics 532, A89.

Li, D., Shields-Zhou, G.A., Ling, H.F., Thirlwall, M., 2011. Dissolutionmethods for strontium isotope stratigraphy: guidelines for the use of bulk carbonate and phosphorite rocks. Chemical Geology 290, 133–144.

Lugli, S., Manzi, V., Roveri, M., Schreiber, B.C., 2010. The Primary Lower Gypsum in the Mediterranean: a newfacies interpretation for the first stage of the Messinian salinity crisis. Palaeogeography, Palaeoclimatology, Palaeoecology 297, 83–99.

Lynch-Stieglitz, J., Stocker, T. F., Broecker, W. S., & Fairbanks, R. G., 1995. The influence of air-sea exchange on the isotopic composition of oceanic carbon: Observations and modeling. Global Biogeochemical Cycles, 9, 653-665.

Manzi, V., Gennari, R., Hilgen, F., Krijgsman, W., Lugli, S., Roveri, M., Sierro, F.J., 2013. Age refinement of the Messinian salinity crisis onset in the Mediterranean. Terra Nova 25, 315–322.

Manzi, V., Gennari, R., Lugli, S., Roveri, M., Schreiber, B.C., 2011. The Messinian “Calcare di Base” (Sicily, Italy) revisited. Geological Society of America Bulletin 123, 347-370.

Manzi, V., Lugli, S., Roveri, M., Dela Pierre, F., Gennari, R., Lozar, F., Natalicchio, M., Schreiber, B.C., Taviani, M., Turco, E., 2016. The Messinian salinity crisis in Cyprus: a further step towards a new stratigraphic framework for Eastern Mediterranean. Basin Research 28, 207-236.

Martin, J.M., Braga, J.C., 1994. Messinian events in the Sorbas basin of Southeastern Spain and their implications of the recent history of the Mediterranean. Sedimentary Geology 90, 257±268.

Mather, A.E., Martín, J.M., Harvey, A.M., Braga, J.C., 2001. A field guide to the Neogene sedimentary basins of the Almeria Province, South-East Spain. Blackwell Science, Oxford, 350 pp.

McArthur, J.M., Howarth, R.J., Bailey, T.R., 2001. Strontium isotope stratigraphy: LOWESS version 3: best fit to the marine Sr-isotope curve for 0–509 Ma and accompanying look-up table for deriving numerical age. Journal of Geology 109, 155–170.

McArthur, J.M., Howarth, R.J., Shields, G.A., 2012. Strontium isotope stratigraphy. In: Gradstein, F.M., Ogg, J.G., Schmitz, M.D., Ogg, G.M., (Eds), The Geological Time Scale 2012. Elsevier B.V., Oxford, pp. 127–144.

McCulloch, M.T., De Deckker, P., 1989. Sr isotope constraints on the Mediterranean environment at the end of the Messinian salinity crisis. Nature 342, 62–65.

McKenzie, J.A., Hodell, D.A., Mueller, P.A., Müller, D.W., 1988. Application of strontium isotopes to late Miocene-early Pliocene stratigraphy. Geology 16, 1022-1025.

Montanari, A., Beaudoin, B., Chan, L.S., Coccioni, R., Deino, A., DePaolo, D.J., Emmanuel, L., Fornaciari, E., Kruge, M., Lundblad, S., Mozzato, C., Portier, E., Renard, M., Rio, D., Sanroni, P., Stankiewicz, A.,

1997. Integrated stratigraphy of the Middle to Upper Miocene pelagic sequence of the Conero Riviera (Marche Region, Italy). In: Montanari, A., Odin, G.S., Coccioni, R. (Eds.), Miocene Stratigraphy: An Integrated Approach. Elsevier Sciences B.V., pp. 409–450.

Montenat, Ch., Ott d'Estevou, P., 1996. Late Neogene basins evolving in the Eastern Betic transcurrent fault zone: an illustrated review. In: Friend, P.F., Dabrio, C.J. (Eds), Tertiary Basins of Spain, the Stratigraphic Record of Crustal Kinematics. Cambridge University Press, Cambridge, pp. 372-286.

Müller, D.W., Mueller, P.A., McKenzie, J.A., 1990. Strontium isotopic ratios as fluid tracers in Messinian evaporites of the Tyrrhenian Sea (Western Mediterranean Sea). Proceeding of the Ocean Drilling Program, Scientific Results 107, 603–614.

Müller, D.W., Mueller, P.A., 1991. Origin and age of the Mediterranean Messinian evaporites: implications from Sr isotopes. Earth and Planetary Science Letters 107, 1–12.

Palmiotto, C., Corda, L., Ligi, M., Cipriani, A., Dick, H.J.B., Douville, E., Gasperini, L., Montagna, P., Thil, F., Borsetti, A.M., Balestra, B., and Bonatti, E., 2013. Nonvolcanic tectonic islands in ancient and modern oceans. Geochemistry, Geophysics, Geosystems 14(10):4698–4717.

Pierre, C., Vangriesheim, A., Laube-Lenfant, E., 1994. Variability of water masses and of organic production-regeneration systems as related to eutrophic, mesotropic and oligotrophic conditions in the northeast Atlantic Ocean. Journal of Marine systems, 5, 159-170.

Pierre, C., 1999. The oxygen and carbon isotope distribution in the Mediterranean water masses. Marine Geology, 153(1), 41-55.

Reinhardt, E.G., Cavazza, W., Patterson, R.T., Blenkinsop, J., 2000. Differential diagenesis of sedimentary components and the implication for strontium isotope analysis of carbonate rocks. Chemical Geology 164, 331–343.

Roveri, M., Flecker, R., Krijgsman, W., Lofi, J., Lugli, S., Manzi, V., Sierro, F.J., Bertini, A., Camerlenghi, A., De Lange, G.J., Govers, R., Hilgen, F.J., Hubscher, C., Meijer, P.Th., Stoica, M., 2014a. The Messinian Salinity Crisis: past and future of a great challenge for marine sciences. Marine Geology 349, 113–125.

Roveri, M., Lugli, S., Manzi, V., Gennari, R., Schreiber, B.C., 2014b. High-resolution strontium isotope stratigraphy of the Messinian deep Mediterranean basins: implications for marginal to central basins correlation. Marine Geology 349, 113–125.

Roveri, M., Manzi, V., Bergamasco, A., Falcieri, F.M., Gennari, R., Lugli, S., Schreiber, B.C., 2014c. Dense shelf water cascading and Messinian canyons: a new scenario for the Mediterranean salinity crisis. American Journal of Science 314, 751-784.

Schildgen, T.F., Cosentino, D., Frijia, G., Castorina, F., Dudas, F.Ö., Iadanza, A., Sampalmieri, G., Cipollari, P., Caruso, A., Bowring, S.A., Strecker, M.R., 2014. Sea level and climate forcing of the Sr isotope composition of late Miocene Mediterranean marine basins. Geochemistry, Geophysics, Geosystems 15, 2964‐2983.

Shackleton, N.J., Hall, M.A., 1997. The Late Miocene stable isotope record, Site 926. In: Shackleton, N.J., Curry, W.B., Richter, C., Bralower, T.J. (Eds.), 1997. Proceedings of the Ocean Drilling Program, scientific results, Vol. 154.

Sierro, F.J., Flores, J.A., Zamarreño, I., Vazquez, A., Utrilla, R., Frances, G., Hilgen, F.J., Krijgsman, W., 1999. Messinian pre-evaporite sapropels and precession-induced oscillations in Western Mediterranean climate. Marine Geology 153, 137–146.

Sierro, F.J., Krijgsman,W., Hilgen, F.J., Flores, J.A., 2001. The Abad composite (SE Spain): a Mediterranean reference section for the Messinian and the Astronomical Polarity Time Scale (APTS). Palaeogeography, Palaeoclimatology, Palaeoecology 168, 143–172.

Sierro, F.J., Flores, J.A., Francés, G., Vazquez, A., Utrilla, R., Zamarreño, I., Erlenkeuser, H., Barcena, M.A., 2003. Orbitally controlled oscillations in planktic communities and cyclic changes in Western Mediterranean hydrography during the Messinian. Palaeogeography, Palaeoclimatology, Palaeoecology 190, 289–316.

Sprovieri, M., Bonanno, A., Barbieri, M., Bellanca, A., Neri, R., Patti, B., Mazzola, S., 2004. $^{87}Sr/^{86}Sr$ variation in Tortonian Mediterranean sediments: a record of Milankovitch cyclicity. In: D'Argenio, B., Fisher, A.G., Premoli Silva, I., Weissert, H., Ferreri, V., (Eds.), Cyclostratigraphy: approaches and case histories. SEPM special publication 81, 17-26.

Topper, R.P.M., Flecker, R.,Meijer, P. Th.,Wortel, M.J.R., 2011. A box model of the Late Miocene Mediterranean Sea: implications from combined $^{87}Sr/^{86}Sr$ and salinity data. Paleoceanography 26, PA3223.
Topper, R.P.M., Meijer, P. Th., 2013. A modelling perspective on spatial and temporal variations in Messinian evaporite deposits. Marine Geology 336, 44–60.
Topper, R.P.M., Lugli, S., Manzi, V., Roveri, M., Meijer, P.Th., 2014. Precessional control of Sr ratios in marginal basins during the Messinian salinity crisis? Geochemistry, Geophysics, Geosystems 15-5, 1926-1944.
Völk, H. R. and Rondeel, H. E., 1964. Zur gliederung des Jungtertiärs im becken von Vera, Südostspanien. Geologie en Mijnbouw 43, 310-315.
Zeebe, R.E., Wolf-Gladrow D.A., 2001. CO_2 in Seawater: Equilibrium, Kinetics, Isotopes. Elsevier Oceanography Series, Amsterdam, 346 pp.

Figure captions

Fig. 1 – A – Stratigraphic framework indicating the three main evolutionary stages of the Messinian salinity crisis (modified after Roveri et al., 2014b). B – Simplified geological map of the Western Mediterranean area, with the location of the Sorbas basin and the studied sections. LY, Los Yesos; RA, Rio de Aguas, PER, Perales composite, H, Hueli, LM, Los Molinos composite section of the PLG unit of Lugli et al. (2010). C – $^{87}Sr/^{86}Sr$ curve during the Messinian salinity crisis in the Mediterranean (modified after Roveri et al., 2014b). PLG, Primary Lower Gypsum; RLG, Resedimented Lower Gypsum; UG, Upper Gypsum; CdB1, CdB2, CdB3 = Calcare di Base facies (Manzi et al., 2011); MES, Messinian erosional surface.

Fig. 2 – Correlation of the Perales composite and Los Molinos sections, with the stratigraphic positions of samples for isotope geochemistry (sections at different scales). The Perales composite section was obtained correlating the upper portion of the Abad composite (Sierro et al., 2001), and the Perales section (Manzi et al., 2013) which includes the Messinian salinity crisis onset. The second gypsum bed was correlated with the base of the Los Molinos section (Yesares Member, Lugli et al., 2010). UA, Upper Abad; PLG, Primary Lower Gypsum.

Fig. 3 – Strontium isotope stratigraphy of the Sorbas basin. The lithological log of the Perales/Los Molinos composite was graphically adapted to the La2010 summer insolation curve at 65°N (Laskar et al., 2011) according to the astronomical tuning proposed by Sierro et al. (2001) for the Upper Abad unit (sapropel midpoint correlated with insolation maxima/humidity peak) and by Lugli et al. (2010) for the PLG unit (banded-branching selenite facies transition correlated with insolation minima/aridity peak).

Fig. 4 – A - $^{87}Sr/^{86}Sr$ values from the pre-MSC interval (Upper Abad interval) and sand-size terrigenous percentages of samples from the entire Abad composite section, plotted against age. Note in particular the decrease of terrigenous input starting across the LA-UA transition (~ 6.7 Ma) and the lowermost $^{87}Sr/^{86}Sr$ high values (red circle), possibly influenced by detrital input of igneous nature into the basin. B - $^{87}Sr/^{86}Sr$ variability of different foraminifer assemblages. The values plotted show the $^{87}Sr/^{86}Sr$ signal of 5 sub-samples of sample MAB5600 (marked by a red square in A), consisting of undifferentiated benthic (B1, B2) and planktonic (P1, P2) taxa and neogloboquadrinids only (N1). C – Strontium isotope values of samples used for reliability test of the $^{87}Sr/^{86}Sr$ signal from foraminifera. Data in parenthesis represent the 2 standard error (2 S.E.) internal uncertainty. (For interpretation of the references to color in this figure legend, the reader is referred to the web version of this article).

Fig. 5 – Oxygen and Carbon isotopes data for the Abad composite section plotted against lithology. Values reported as $\delta^{18}O$ and $\delta^{13}C$ per mil relative to Vienna Pee Dee Belemnite (VPDB) by assigning a $\delta^{13}C$ value of +1.95‰ and a $\delta^{18}O$ value of -2.20‰ to NBS 19. The overall external analytical precision based on replicate analysis of laboratory standards was better than ± 0.23 ‰ for $\delta^{18}O$ and ± 0.10 ‰ for $\delta^{13}C$. Values referred to *O. universa* and *G. bulloides* are from Sierro et al., 2003).

Fig. 6 – Scanning electron micrograph (SEM) of Neogloboquadrina specimens from sample PER 2270 and MAB 5600 (relative stratigraphic positions and stable isotopes values are indicated in Fig. 5). (a, e, i) and (b,

f, l) refer respectively to unleached and leached sample PER 2270, while (c, g, m) and (d, h, n) refer respectively to unleached and leached sample MAB 5600.

Fig. 7 –Oscillations of isotopic values on different orbital time scales for the Sorbas basin. A – $^{87}Sr/^{86}Sr$, $\delta^{18}O$ and $\delta^{13}C$ precessional scale oscillations, exemplarily shown for cycles UA18-21. Note the climate-driven variability of the geochemical proxies for the different facies of a single cycle. B – Long-term trend of $^{87}Sr/^{86}Sr$ values for precession maxima intervals, showing cyclical oscillations with a period of 400 kyr.

Table captions

Table 1: Samples information and results of the geochemical analyses. An asterisk indicates samples consisting of diverse foraminifer taxa and not of only neogloboquadrinid specimens. Ages of individual samples were obtained by the astronomical tuning proposed by Sierro et al. (2001) for the Abad composite and by Lugli et al. (2010) for the Los Molinos sections. For $^{87}Sr/^{86}Sr$ data, values in parenthesis represent the 2 standard error (2 S.E.) internal uncertainty. Oxygen and carbon data are reported as $\delta^{18}O$ and $\delta^{13}C$ per mil relative to Vienna Pee Dee Belemnite (VPDB) by assigning a $\delta^{13}C$ value of +1.95‰ and a $\delta^{18}O$ value of -2.20‰ to NBS 19. The overall external analytical precision based on replicate analysis of laboratory standards was better than ± 0.23 ‰ for $\delta^{18}O$ and ± 0.10 ‰ for $\delta^{13}C$.

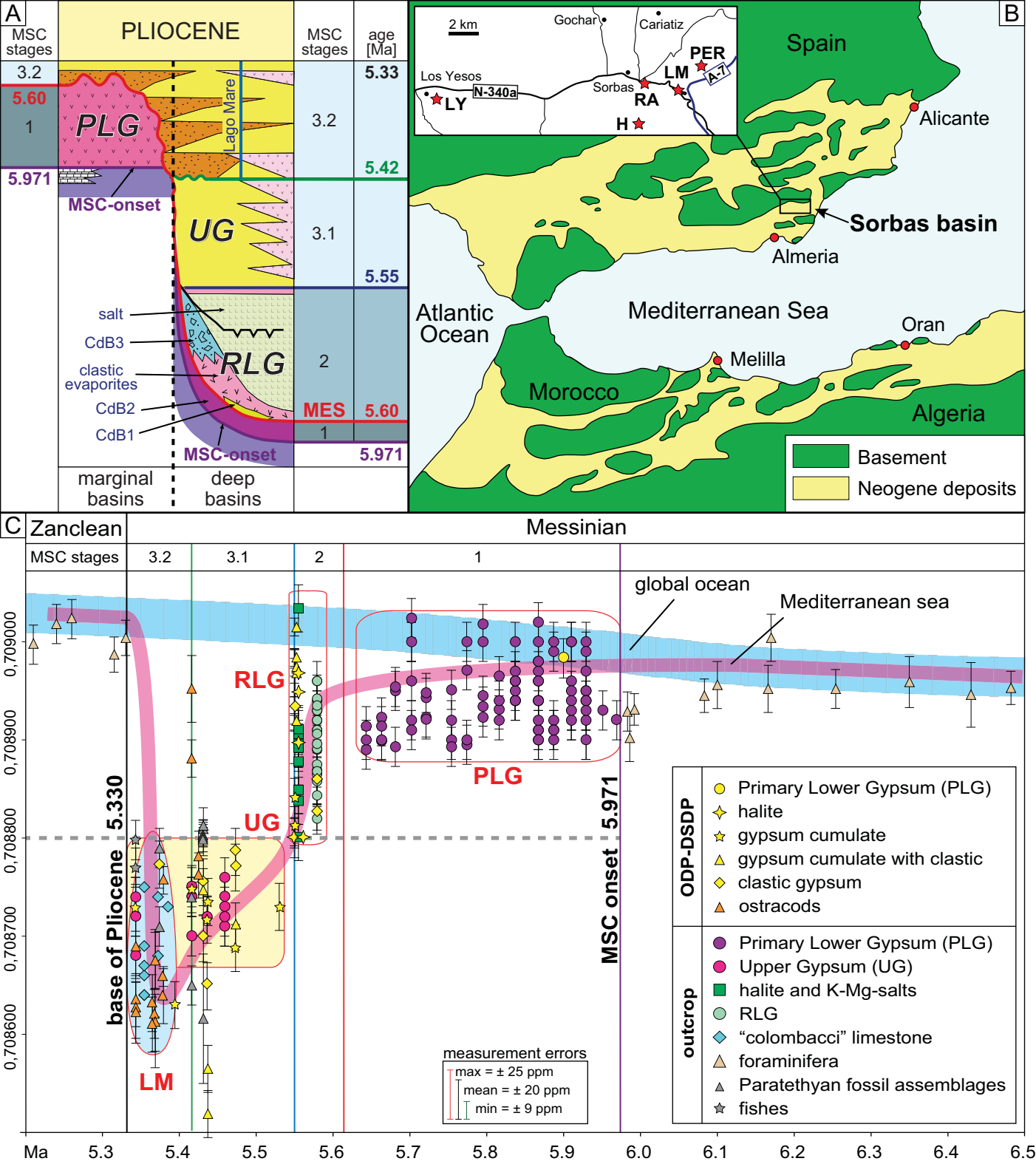
A
MSC stages
PLIOCENE
MSC stages
age [Ma]
3.2
5.60
1
5.971
PLG
Lago Mare
MSC-onset
UG
3.1
5.33
5.42
5.55
salt
CdB3
clastic evaporites
CdB2
CdB1
RLG
2
MES
5.60
1
MSC-onset
5.971
marginal basins
deep basins
B
2 km
Gochar
Cariatiz
PER
LM
A-7
Los Yesos
N-340a
LY
Sorbas
RA
H
Spain
Alicante
Sorbas basin
Almeria
Atlantic Ocean
Mediterranean Sea
Oran
Melilla
Morocco
Algeria
Basement
Neogene deposits
C
Zanclean
Messinian
MSC stages
3.2
3.1
2
1
global ocean
Mediterranean sea
RLG
PLG
UG
LM
5.330
base of Pliocene
5.971
MSC onset
0,709000
0,708900
0,708800
0,708700
0,708600
measurement errors
max = ± 25 ppm
mean = ± 20 ppm
min = ± 9 ppm
ODP-DSDP
Primary Lower Gypsum (PLG)
halite
gypsum cumulate
gypsum cumulate with clastic
clastic gypsum
ostracods
outcrop
Primary Lower Gypsum (PLG)
Upper Gypsum (UG)
halite and K-Mg-salts
RLG
“colombacci” limestone
foraminifera
Paratethyan fossil assemblages
fishes
Ma
5.3
5.4
5.5
5.6
5.7
5.8
5.9
6.0
6.1
6.2
6.3
6.4
6.5

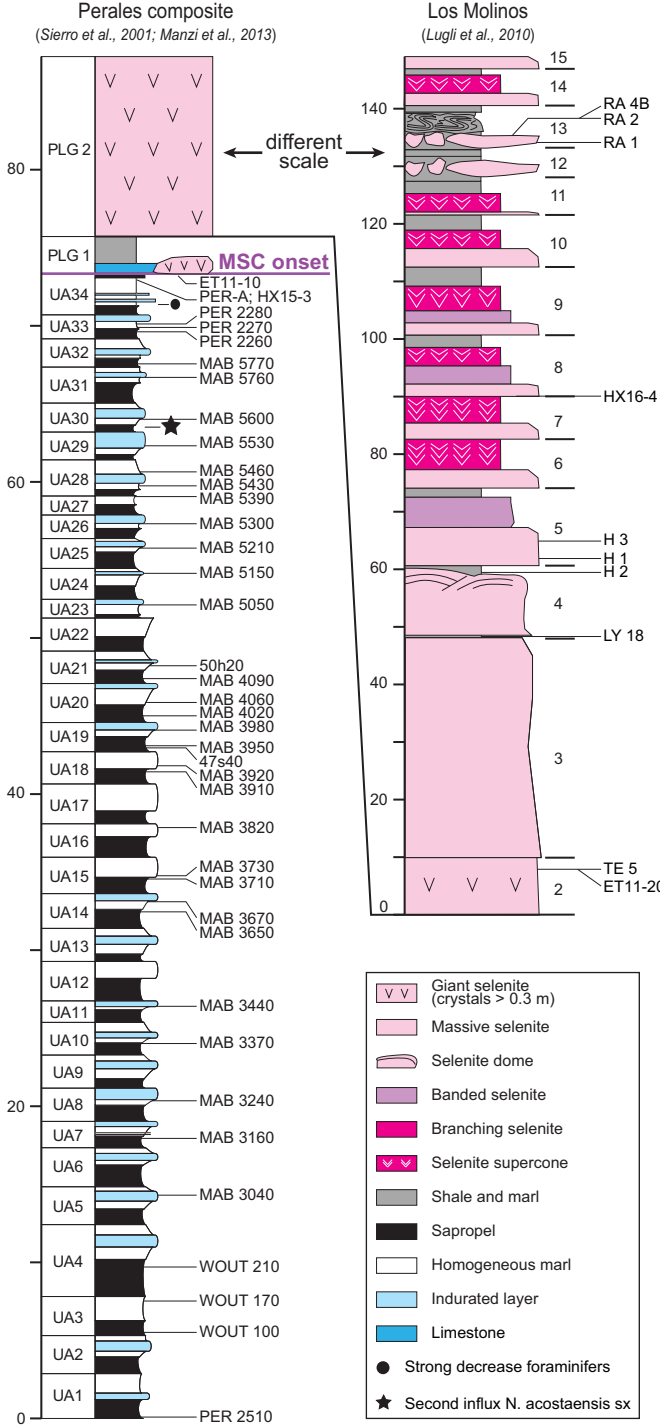
Perales composite
(Sierro et al., 2001; Manzi et al., 2013)
Los Molinos
(Lugli et al., 2010)
different scale
PLG 2
PLG 1
MSC onset
UA34
UA33
UA32
UA31
UA30
UA29
UA28
UA27
UA26
UA25
UA24
UA23
UA22
UA21
UA20
UA19
UA18
UA17
UA16
UA15
UA14
UA13
UA12
UA11
UA10
UA9
UA8
UA7
UA6
UA5
UA4
UA3
UA2
UA1
ET11-10
PER-A; HX15-3
PER 2280
PER 2270
PER 2260
MAB 5770
MAB 5760
MAB 5600
MAB 5530
MAB 5460
MAB 5430
MAB 5390
MAB 5300
MAB 5210
MAB 5150
MAB 5050
50h20
MAB 4090
MAB 4060
MAB 4020
MAB 3980
MAB 3950
47s40
MAB 3920
MAB 3910
MAB 3820
MAB 3730
MAB 3710
MAB 3670
MAB 3650
MAB 3440
MAB 3370
MAB 3240
MAB 3160
MAB 3040
WOUT 210
WOUT 170
WOUT 100
PER 2510
0
20
40
60
80
15
14
13
12
11
10
9
8
7
6
5
4
3
2
140
120
100
80
60
40
20
0
RA 4B
RA 2
RA 1
HX16-4
H 3
H 1
H 2
LY 18
TE 5
ET11-20
Giant selenite (crystals > 0.3 m)
Massive selenite
Selenite dome
Banded selenite
Branching selenite
Selenite supercone
Shale and marl
Sapropel
Homogeneous marl
Indurated layer
Limestone
Strong decrease foraminifers
Second influx N. acostaensis sx

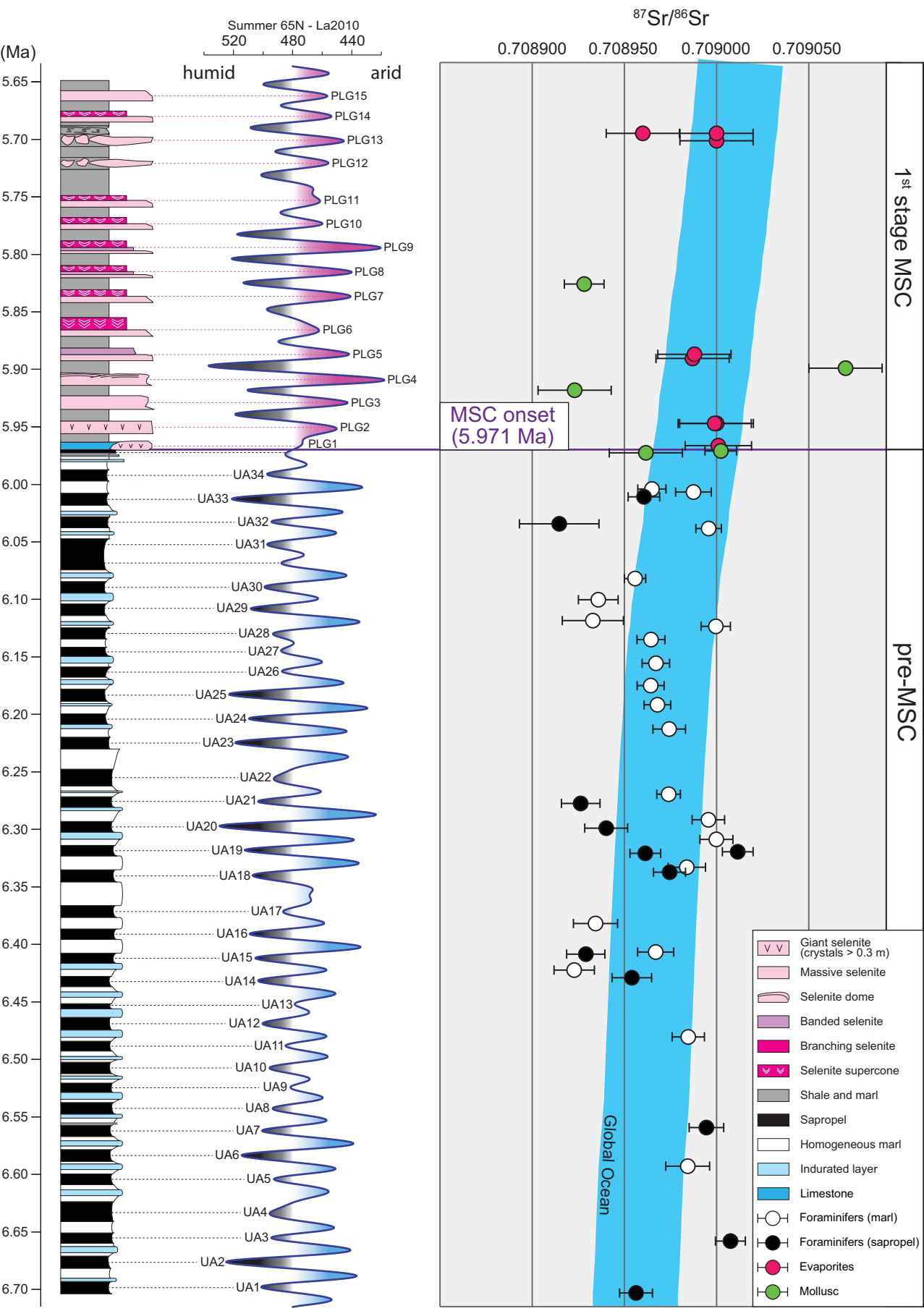
(Ma)
Summer 65N - La2010
520
480
440
humid
arid
5.65
5.70
5.75
5.80
5.85
5.90
5.95
6.00
6.05
6.10
6.15
6.20
6.25
6.30
6.35
6.40
6.45
6.50
6.55
6.60
6.65
6.70
PLG15
PLG14
PLG13
PLG12
PLG11
PLG10
PLG9
PLG8
PLG7
PLG6
PLG5
PLG4
PLG3
PLG2
PLG1
UA34
UA33
UA32
UA31
UA30
UA29
UA28
UA27
UA26
UA25
UA24
UA23
UA22
UA21
UA20
UA19
UA18
UA17
UA16
UA15
UA14
UA13
UA12
UA11
UA10
UA9
UA8
UA7
UA6
UA5
UA4
UA3
UA2
UA1
87Sr/86Sr
0.708900
0.708950
0.709000
0.709050
MSC onset
(5.971 Ma)
1st stage MSC
pre-MSC
Global Ocean
Giant selenite
(crystals > 0.3 m)
Massive selenite
Selenite dome
Banded selenite
Branching selenite
Selenite supercone
Shale and marl
Sapropel
Homogeneous marl
Indurated layer
Limestone
Foraminifers (marl)
Foraminifers (sapropel)
Evaporites
Mollusc

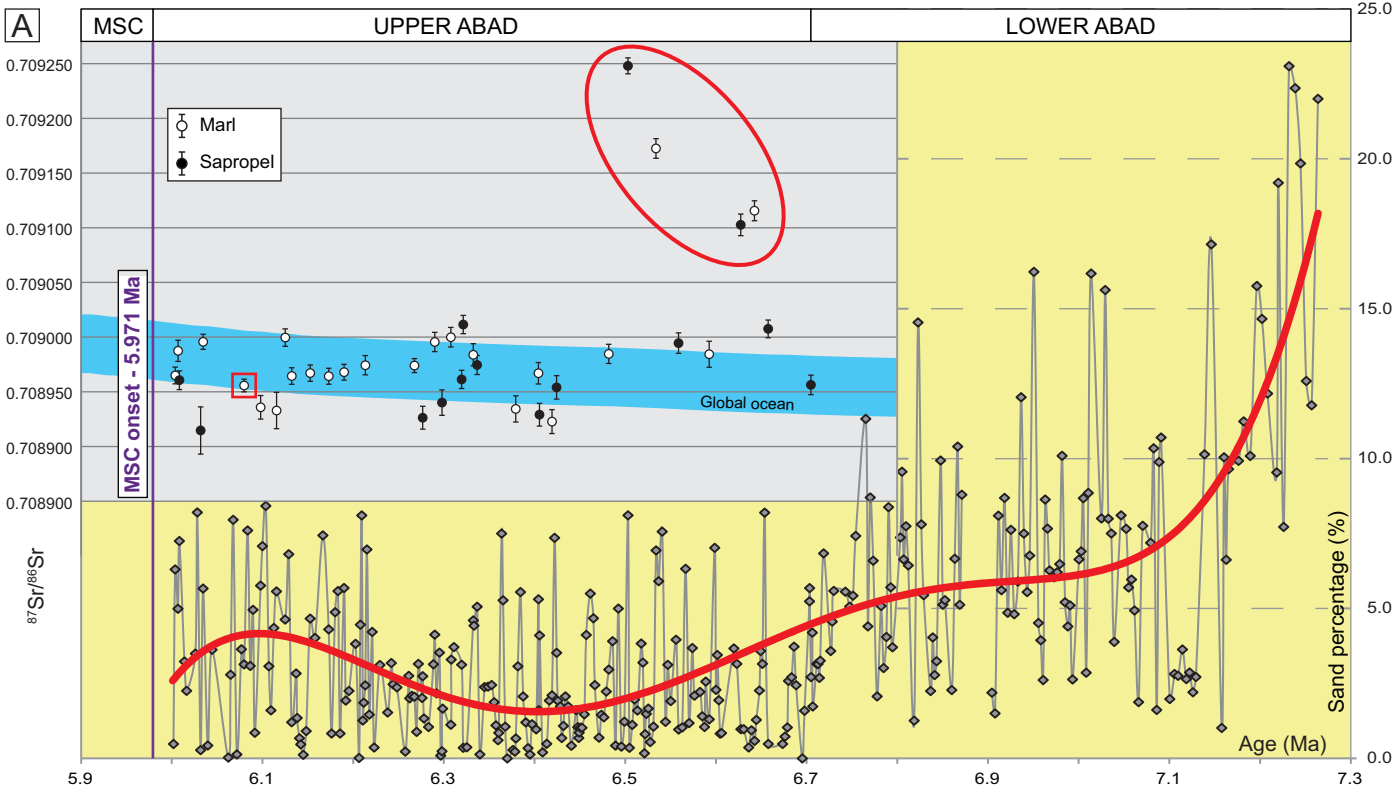

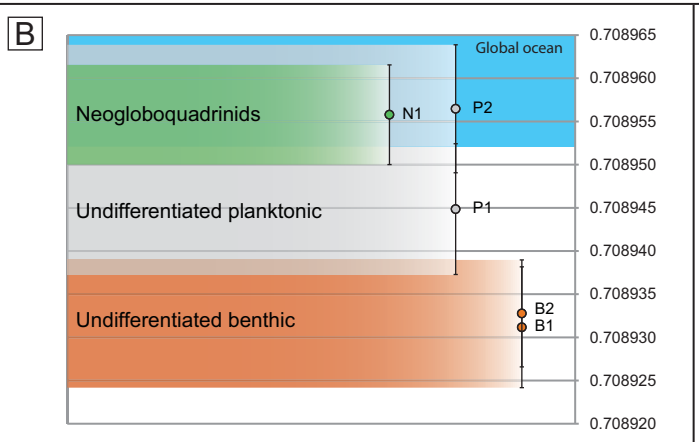

C

$^{87}Sr/^{86}Sr$ table results

Sample	Depth (m)	Age (kyr)	Cycle	$^{87}Sr/^{86}Sr$
N1	109.87	6079.8	UA30	0.708956 (6)
P1	109.87	6079.8	UA30	0.708945 (8)
P2	109.87	6079.8	UA30	0.708956 (7)
B1	109.87	6079.8	UA30	0.708931 (7)
B2	109.87	6079.8	UA30	0.708933 (6)

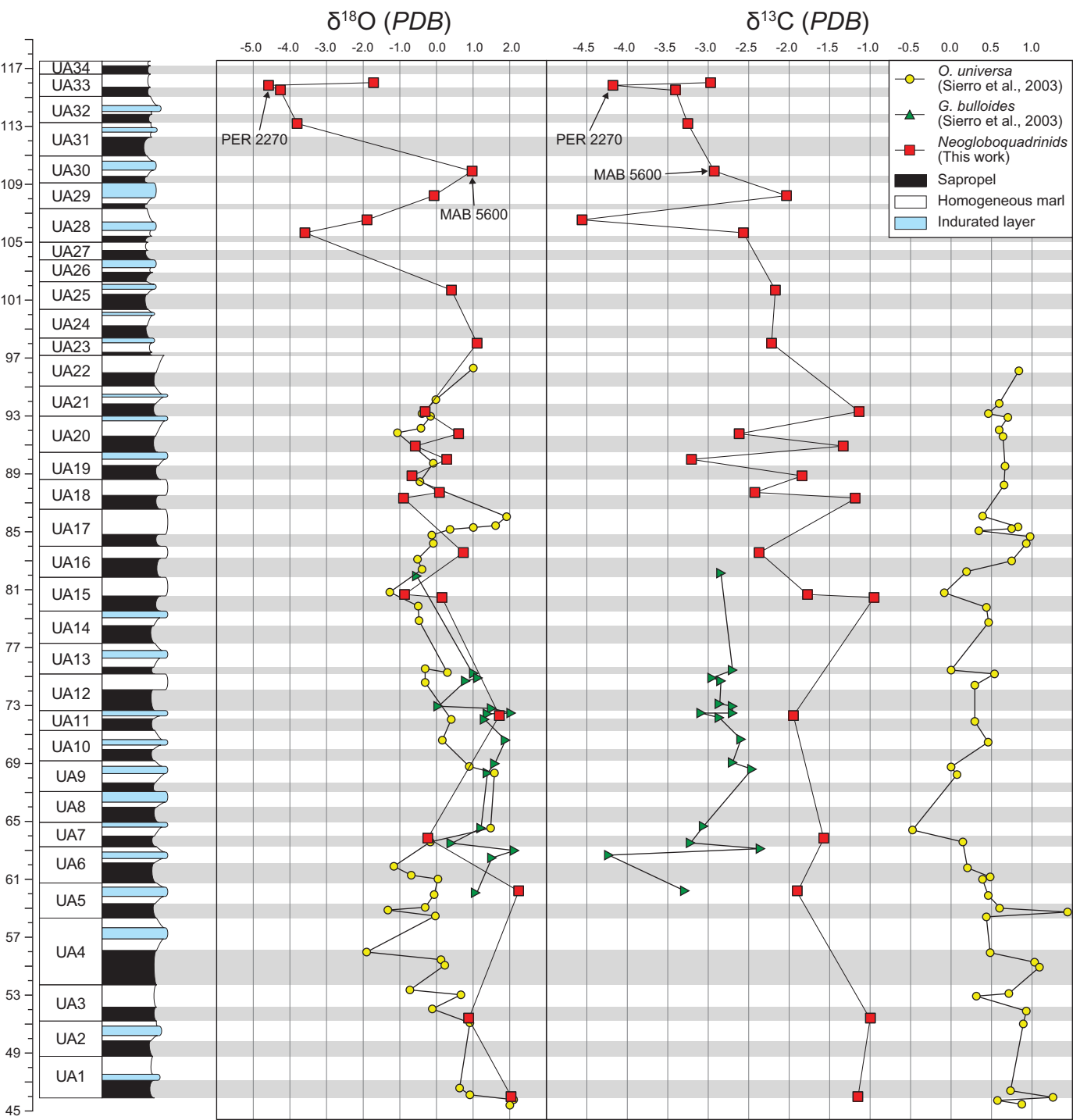
δ18O (PDB)
δ13C (PDB)
-5.0 -4.0 -3.0 -2.0 -1.0 0.0 1.0 2.0
-4.5 -4.0 -3.5 -3.0 -2.5 -2.0 -1.5 -1.0 -0.5 0.0 0.5 1.0
117 113 109 105 101 97 93 89 85 81 77 73 69 65 61 57 53 49 45
UA34 UA33 UA32 UA31 UA30 UA29 UA28 UA27 UA26 UA25 UA24 UA23 UA22 UA21 UA20 UA19 UA18 UA17 UA16 UA15 UA14 UA13 UA12 UA11 UA10 UA9 UA8 UA7 UA6 UA5 UA4 UA3 UA2 UA1
PER 2270
MAB 5600
PER 2270
MAB 5600
O. universa (Sierro et al., 2003)
G. bulloides (Sierro et al., 2003)
Neogloboquadrinids (This work)
Sapropel
Homogeneous marl
Indurated layer

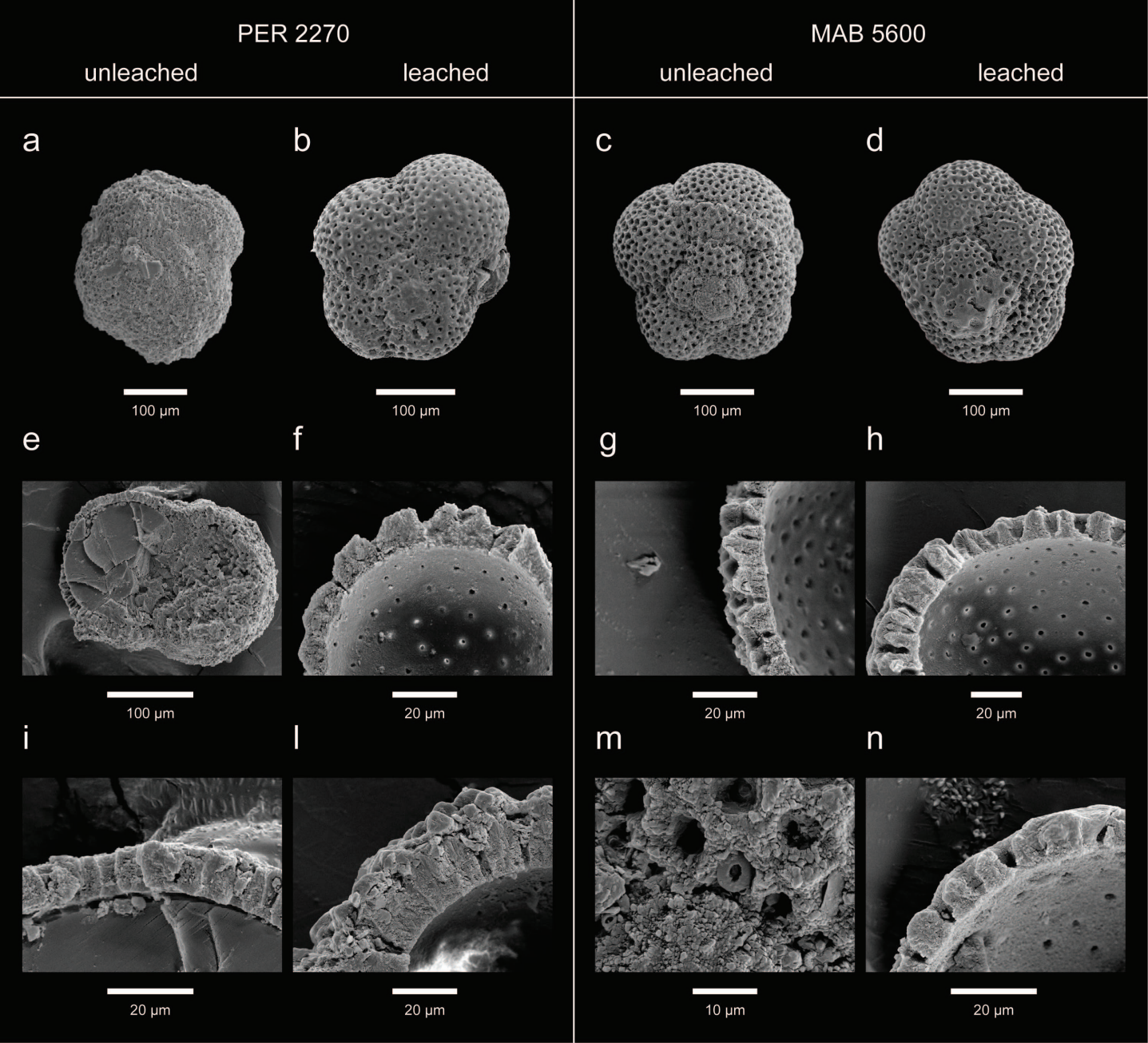
PER 2270
unleached
leached
MAB 5600
unleached
leached
a
b
c
d
100 µm
100 µm
100 µm
100 µm
e
f
g
h
100 µm
20 µm
20 µm
20 µm
i
l
m
n
20 µm
20 µm
10 µm
20 µm

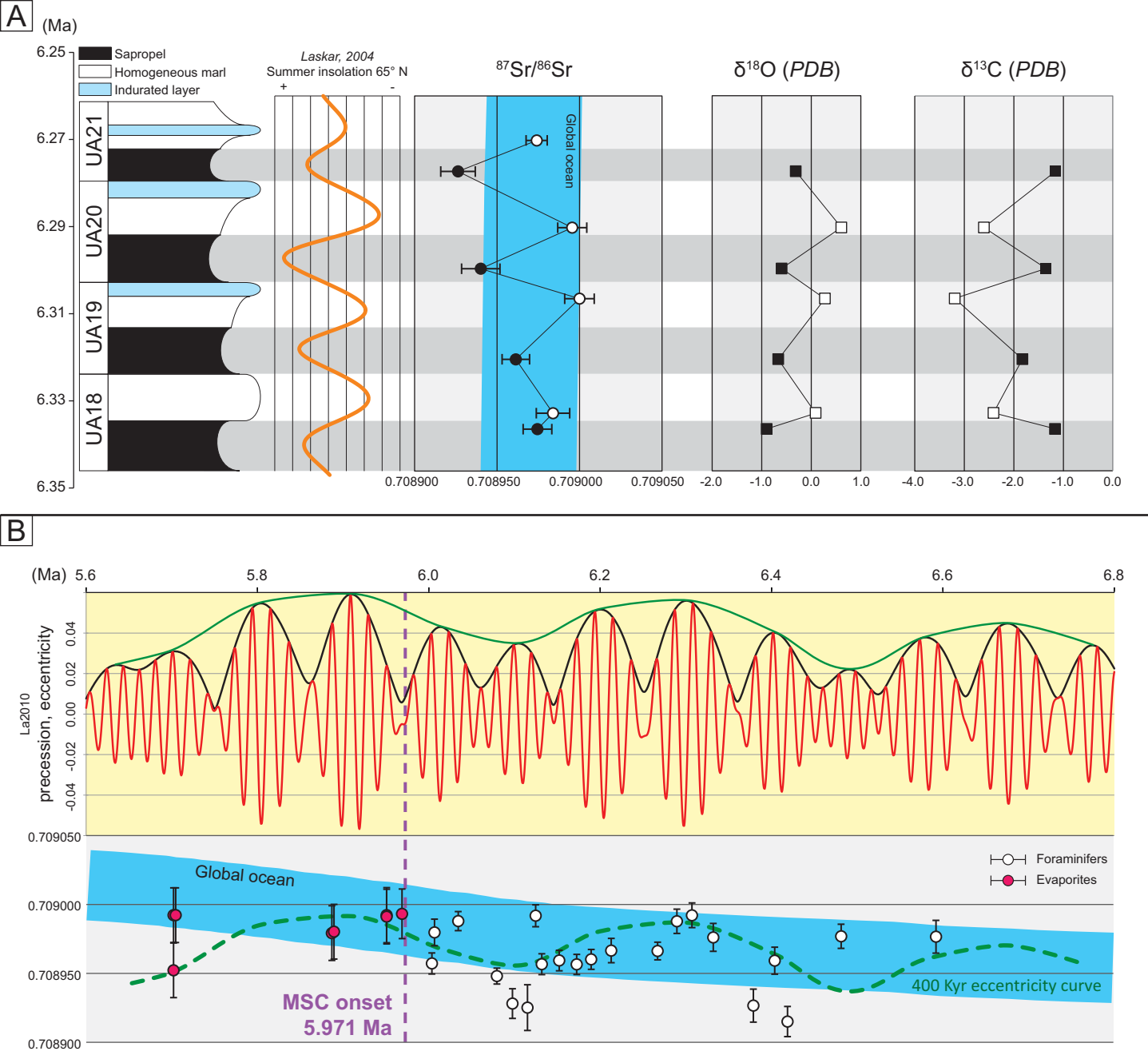
A
(Ma)
Sapropel
Homogeneous marl
Indurated layer
Laskar, 2004
Summer insolation 65° N
+
-
87Sr/86Sr
δ18O (PDB)
δ13C (PDB)
Global ocean
UA21
UA20
UA19
UA18
6.25
6.27
6.29
6.31
6.33
6.35
0.708900
0.708950
0.709000
0.709050
-2.0
-1.0
0.0
1.0
-4.0
-3.0
-2.0
-1.0
0.0
B
(Ma)
5.6
5.8
6.0
6.2
6.4
6.6
6.8
La2010
precession, eccentricity
0.04
0.02
0.00
-0.02
-0.04
0.709050
0.709000
0.708950
0.708900
Global ocean
Foraminifers
Evaporites
400 Kyr eccentricity curve
MSC onset
5.971 Ma

Sample	Section	Age (kyr)	Cycle	Depth (m)	Lithofacies/type	$^{87}Sr/^{86}Sr$	$\delta^{18}O$ (‰)	$\delta^{13}C$ (‰)
RA 1	Rio Aguas	5708.0	PLG13		Massive selenite	0.709000 (20)		
RA 2	Rio Aguas	5702.0	PLG13		Branching selenite	0.709000 (20)		
RA 4B	Rio Aguas	5702.0	PLG13		Branching selenite	0.708960 (20)		
HX16-4	Hueli	5837.0	PLG8		Mollusk shell	0.708928 (11)		
H1	Hueli	5887.0	PLG5		Limestone	0.708987 (20)		
H3	Hueli	5887.0	PLG5		Massive selenite	0.708988 (20)		
H2	Hueli	5887.0	PLG5		Mollusk shell	0.709071 (13)		
LY 18	Los Yesos	5910.0	PLG4		Mollusk shell	0.708921 (16)		
TE 5	Perales	5951.0	PLG2		Massive selenite	0.709000 (20)		
ET-11-20	Perales	5951.0	PLG2		Massive selenite	0.708999 (20)		
ET-11-10	Perales	5969.0	PLG1		Massive selenite	0.709001 (18)		
HX15-3	Hueli	5969.0	PLG1		Mollusk shell	0.709002 (9)		
PER-A	Perales	5983.0	UA34		Mollusk shell	0.708958 (20)		
PER-2280	Perales	6003.8	UA33	115.95	Marl	0.708965 (8)	-1.72	-2.98
PER-2270	Perales	6006.9	UA33	115.71	Marl	0.708987 (10)	-4.58	-4.19
PER-2260	Perales	6008.4	UA33	115.59	Sapropel	0.708961 (9)	-4.26	-3.41
MAB-5770	Perales	6031.8	UA32	113.47	Sapropel	0.708915 (22)		
MAB-5760*	Perales	6034.5	UA 31	113.24	Marl	0.708996 (7)	-3.80	-3.26
MAB-5600	Perales	6079.8	UA30	109.87	Marl	0.708956 (6)	0.97	-2.93
MAB-5530	Perales	6098.0	UA 29	108.32	Marl	0.708936 (11)	-0.07	-2.04
MAB-5460	Perales	6115.5	UA28	106.59	Marl	0.708933 (17)	-1.89	-4.57
MAB-5430	Perales	6125.1	UA28	105.64	Marl	0.709000 (8)	-3.59	-2.57
MAB-5390*	Perales	6132.2	UA27	104.97	Marl	0.708964 (8)		
MAB-5300*	Perales	6152.6	UA26	103.32	Marl	0.708967 (7)		
MAB-5210	Perales	6173.1	UA25	101.67	Marl	0.708964 (7)	0.44	-2.18
MAB-5150*	Perales	6190.0	UA24	100.11	Marl	0.708968 (7)		
MAB-5050	Perales	6213.4	UA23	98.04	Marl	0.708974 (9)	1.11	-2.23
50h20*	Perales	6267.6	UA21	94.22	Marl	0.708974 (6)		
MAB-4090	Perales	6276.8	UA21	93.29	Sapropel	0.708926 (10)	-0.31	-1.14
MAB-4060	Perales	6290.0	UA20	91.78	Marl	0.708996 (9)	0.60	-2.63
MAB-4020	Perales	6298.0	UA20	90.92	Sapropel	0.708940 (12)	-0.60	-1.34
MAB-3980	Perales	6307.7	UA19	90.04	Marl	0.709000 (9)	0.27	-3.22
MAB-3950*	Perales	6319.6	UA19	88.95	Sapropel	0.708961 (8)		
47s40*	Perales	6321.4	UA19	88.78	Sapropel	0.709012 (8)	-0.67	-1.85
MAB-3920	Perales	6332.5	UA18	87.73	Marl	0.708984 (10)	0.09	-2.43
MAB-3910	Perales	6336.8	UA18	87.33	Sapropel	0.708974 (9)	-0.90	-1.19
MAB-3820	Perales	6379.4	UA16	83.57	Marl	0.708934 (12)	0.73	-2.38
MAB-3730	Perales	6404.3	UA15	80.70	Marl	0.708967 (10)	-0.87	-1.78
MAB-3710	Perales	6405.6	UA15	80.54	Sapropel	0.708929 (10)	0.15	-0.96
MAB-3670	Perales	6419.3	UA14	79.01	Marl	0.708923 (11)		
MAB-3650	Perales	6424.4	UA14	78.47	Sapropel	0.708954 (11)		
MAB-3440	Perales	6481.9	UA11	72.20	Marl	0.708985 (9)	1.72	-1.96
MAB-3370	Perales	6503.1	UA10	69.97	Sapropel	0.709248 (7)		
MAB-3240	Perales	6534.1	UA8	66.21	Marl	0.709173 (9)		
MAB-3160	Perales	6558.9	UA7	63.87	Sapropel	0.708995 (9)	-0.24	-1.58
MAB-3040	Perales	6592.7	UA5	60.18	Marl	0.708984 (12)	2.25	-1.91
WOUT-210	Perales	6627.5	UA4	55.66	Sapropel	0.709103 (10)		
WOUT-170	Perales	6642.7	UA3	53.46	Marl	0.709116 (9)		
WOUT-100	Perales	6657.8	UA3	51.33	Sapropel	0.709008 (8)	0.88	-1.00
PER-2510	Perales	6705.0	UA1	45.93	Sapropel	0.708956 (9)	2.03	-1.16